Politecnico di Torino

POLITECNICO DI TORINO

DEPARTMENT OF MECHANICAL AND AEROSPACE ENGINEERING

Master's Thesis

Numerical Analysis of Printability and Microstructure of Directed Energy Deposited H13-IN718 Multi-Material

Fatemeh Parsa

s310253

Supervisor: Prof. Abdollah Saboori

Co-Supervisor: Dr. Reza Ghanavati

July 2026

Abstract

Directed Energy Deposition (DED) is one of the most important metal additive manufacturing technologies, used for fabrication and repair of structurally and compositionally complex parts. In the present thesis, a transient thermal numerical model of a multi-material DED process was developed using the finite element method (FEM). The study focused on the sequential deposition of H13 tool steel and Inconel 718 (IN718) on a substrate using the element activation/deactivation (birth/death) technique. A transient heat transfer analysis was implemented to investigate the temperature distribution during the deposition process, and then to evaluate the printability and solidification characteristics across the multi-material part. The numerical framework was inspired by previous studies in our team on multi-material DED and was adapted to the specific geometry, material combination and process conditions investigated in this thesis. The finite element model was created in Abaqus/CAE and modified through the input (*.inp) file to implement element activation with the *Model Change command and a moving volumetric heat source through a DFLUX user subroutine. Fourteen deposition layers were modeled; the lower seven layers and the substrate consisted of H13 and the upper seven layers of IN718. The model included transient heat transfer, an effective surface-film boundary condition combining convection and radiation, a moving Goldak double-ellipsoidal heat source, and temperature-dependent material properties, with the thermal conductivity enhanced above the solidus to represent melt-pool convection.

The simulated thermal history showed a progressive heat accumulation along the build: the layer peak temperature rose from about 1822 °C in the first layer to about 2472 °C at the top of the H13 section, and settled at a quasi-steady 2110–2180 °C through the IN718 layers. The printability analysis predicted sound interlayer bonding over the whole wall except at the first layer, whose lack-of-fusion ratio of 0.75 indicates a bonding risk at the substrate interface; the thermal-strain susceptibility ε^* reached its maximum at the final deposited layer; and the composition change by selective vaporization remained limited, with a maximum chromium loss of about 9 % in the IN718 section and a manganese loss of no more than about 6.3 % in the H13 section. The solidification analysis gave cooling rates decreasing from about 1695 °C/s to 154 °C/s up the build, secondary dendrite arm spacings coarsening from about 6.9 µm in H13 to 8.8 µm in IN718, and a morphology ratio G/R falling from about 27 to about 1 °C·s·mm^{-2}, indicating a cellular/dendritic H13 section and a fully dendritic IN718 section whose structure coarsens toward the top of the part.

Acknowledgment

I am deeply grateful to my supervisor and my academic advisors for their guidance, excellent suggestions and strong support during the course of this research. Their knowledge, support and constructive criticism have been important to the effective completion of this thesis.

I would also like to further recognize the authors and researchers whose published work provided the scientific basis and motivation for the numerical framework established in this study. Their contribution in additive manufacturing and numerical modeling has been considerable and has greatly supported this research.

I would like to end by thanking my family for their constant support, patience and understanding during this journey. Special thanks to my husband whose love, encouragement and unfailing belief in me has been my greatest source of strength and motivation.

Table of Contents

1 Introduction

Additive manufacturing is now one of the most disruptive technologies in the modern manufacturing industry. Directed Energy Deposition (DED) is one of the various additive manufacturing techniques that has attracted considerable interest due to its ability to manufacture large-scale metallic components, repair damaged structures and produce tailored materials for multi-functional applications.

DED processing involves deposition of metallic material in layers, with a high-energy heat source, usually a laser, being used simultaneously. The localized heat input melts the material and a molten pool is generated that solidifies rapidly. The thermal history during this process has a strong influence on the final mechanical properties, residual stresses, microstructure and dimensional accuracy.

Multi-material additive manufacturing has gained importance in recent years as it enables engineers to combine different materials in a single component. These structures may have enhanced resistance to thermal stress and wear and mechanical performance.

The present thesis deals with the numerical simulation of a multi-material DED process of H13 tool steel and IN718. H13 is a commonly used tool steel for tooling applications owing to its hardness and thermal-fatigue resistance, whereas IN718 is a nickel-based superalloy known for its high-temperature strength and corrosion resistance. The main goal is to develop a transient thermal finite element model in Abaqus to simulate the sequential layer deposition process using the birth and death method, and then to analyze printability and solidification parameters across the multi-material part based on the temperature fields as inputs into analytical equations.

The specific objectives of the thesis are:

- Development of a thermal finite element model of the DED process.
- Implementation of element activation/deactivation through input-file editing for sequential deposition of the 14-layer H13-IN718 multi-material.
- Implementation of a moving Goldak heat source through a DFLUX user subroutine.
- Investigation of printability indexes, including lack of fusion, thermal strain, and composition change defects across the multi-material.
- Evaluation of the solidification behavior based on the temperature gradients (G) and solidification rates (R) across the multi-material.

The simulation framework developed in this work can later be extended to include residual-stress prediction, distortion analysis, and microstructure evolution.

2 Literature Review

2.1 Additive Manufacturing

Additive manufacturing (AM) is a process where parts are created by adding material layer by layer from a 3D digital representation of a component. This is in contrast to subtractive manufacturing where material is removed from a larger billet. Over the last two decades, AM has shifted from rapid prototyping to direct production of functional, end-use parts, standardized by ASTM/ISO into seven process categories — binder jetting, directed energy deposition, material extrusion, material jetting, powder-bed fusion, sheet lamination and vat photopolymerization. Its main benefits include the ability to produce very complex and topology-optimized geometries that are difficult or impossible to machine, significant reduction of material waste, consolidation of multi-part assemblies into single components and short, tool-free lead times that enable on-demand production. [1]

The most developed processes for metallic materials belong to two families:

- Powder-bed fusion (PBF) processes involve spreading a thin layer of powder and then selectively melting it using a laser (selective laser melting, SLM, or direct metal laser sintering) or an electron beam (electron-beam melting, EBM). These offer fine resolution and good surface finish and are commonly used for making complex aerospace and biomedical parts. [2]

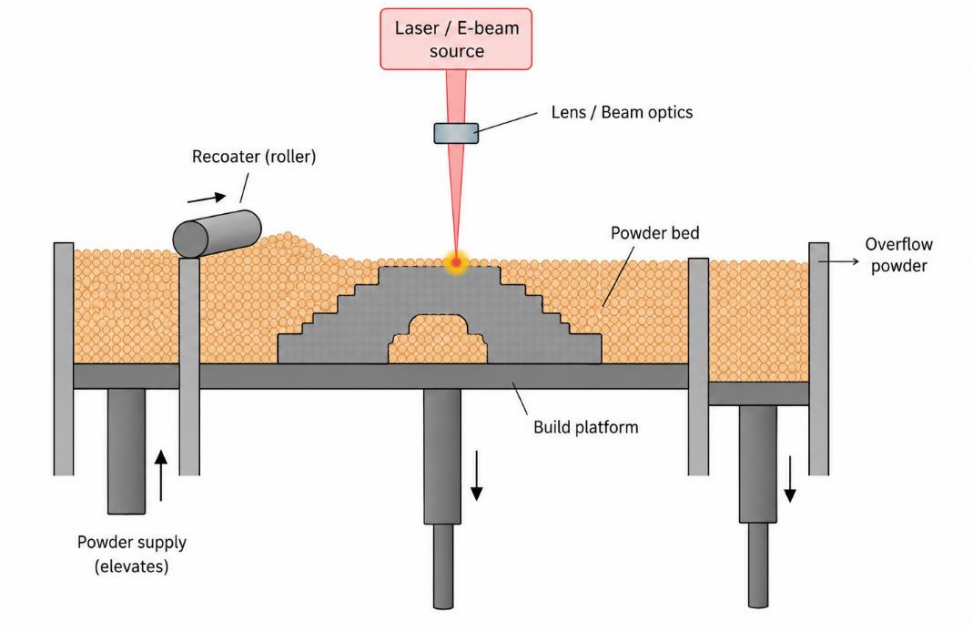

Figure 2.1. *schematic of the powder-bed fusion process*

- Directed energy deposition (DED), or laser metal deposition (LMD) or wire-arc additive manufacturing when an arc source is used, is when the feedstock is melted as it is fed to the deposition point. DED is more suited to larger components, higher build rates and the repair of existing parts.

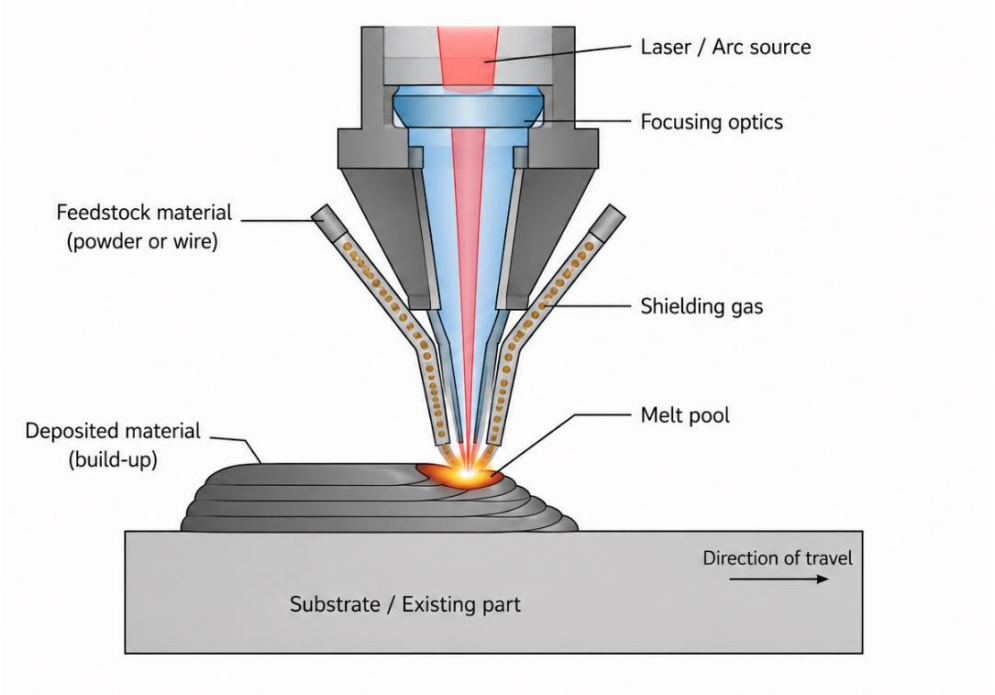

Figure 2.2. *schematic of the DED process*

Another metal route is via binder jetting where a liquid binder is selectively deposited on a powder bed prior to a separate sintering step. All of these processes generate the part by local addition and solidification of material and are repeated many times. As a consequence, they all impose strong, spatially and temporally varying thermal cycles on the workpiece. It is the thermal cycles which ultimately control the microstructure, the residual stresses and the dimensional accuracy of the finished part.

2.2 Directed Energy Deposition

Directed Energy Deposition is an additive manufacturing process in which a high energy source, usually a laser, creates a small melt pool on a substrate or previously deposited material while metallic powder or wire is fed directly into that melt pool. The source and the deposition head travel along a pre-programmed toolpath, melting and fusing material exactly where the beam is focused. Typically, the powder is carried and shielded by an inert gas. A part is constructed by laying down adjacent tracks to create a layer, and building up successive layers. In contrast to powder-bed fusion, where the feedstock is supplied and melted from a pre-spread bed, DED has the ability to offer a large build envelope and high deposition rates, the ability

to repair existing parts and the ability to change the feedstock during the build to create multi-material structures. [3] This process couples several phenomena operating on very different scales. Some of the incident energy is absorbed and increases the surface above its melting point. [4] Within the resulting pool, surface-tension and buoyancy-driven flows redistribute heat far more effectively than conduction alone. This is why the present model raises the effective conductivity above the solidus to represent this stirring. As the source moves, the pool solidifies quickly creating the fine microstructures associated with additive manufacturing. Heat dissipates mainly conduction-wise into the substrate and below layers. Since the source is localized and moving, each point undergoes repeated heating-and-cooling cycles. As the wall grows, the conduction path to the substrate becomes longer, so the upper layers cool less efficiently and the average temperature rises — an effect known as heat accumulation, examined in detail for the present build in Section 8.1.2. The laser power, scan speed, layer thickness and beam size control this transient thermal field, which governs the melt-pool dimensions and the eventual residual stresses, and it is the central aim of this work to replicate this field.

One of the specificities of DED is the possibility to join dissimilar metals, here a thermal-fatigue resistant tool steel and a high temperature nickel superalloy, whose different conductivities and melting ranges modify the heat flow across the transition and makes the thermal field close to the H13-IN718 interface of particular interest. The resolution of all coupled phenomena is prohibitive for a multi-layer build, thus here the process is reduced to a transient thermal finite element analysis where the laser is a moving volumetric heat source, material addition is reproduced by element activation, melt-pool convection is approximated by the enhanced above-solidus conductivity, and surface losses are lumped into an effective film coefficient.

2.3 Numerical Modeling of DED

Finite element modeling has become the standard approach for analyzing DED, because it gives access to the full transient temperature, stress and strain fields that are hard to measure experimentally and allows process parameters to be explored without repeated trials. [5] Reported studies span a range of objectives, including thermal analysis, thermo-mechanical analysis for residual stress and distortion, melt-pool and fluid-flow modeling, and the prediction of microstructure. Among these, the transient thermal analysis is usually the first step and the foundation for the others, since the temperature distribution governs the melt-pool geometry, the solidification conditions and the thermal stresses that develop subsequently.

A central element of any such model is the representation of the moving heat source. Early analyzes relied on the analytical moving point- and line-source solutions of Rosenthal, but these neglect the finite size of the source and are inaccurate near the melt pool. Distributed descriptions are therefore preferred: a Gaussian surface flux represents the laser as a two-dimensional heat input, while Goldak's double-ellipsoidal model distributes the heat over a three-dimensional volume with separate leading and trailing lengths and has become the most widely adopted source for welding and DED because it reproduces both the shape and the penetration of the melt pool. [6] In finite element codes the moving source is commonly applied through a user subroutine, such as DFLUX in Abaqus, that evaluates the volumetric flux as a function of position and time. Equally important is the treatment of the material: the thermophysical properties are taken as temperature dependent, the latent heat of fusion is incorporated through the enthalpy method, and the thermal conductivity is frequently increased above the liquidus, or solidus, to account in an averaged way for the convective heat transport within the melt pool that a purely conductive model would otherwise miss. [7] Models also differ in scale, from melt-pool-resolved simulations that capture the fluid dynamics of a single track to the part-scale, layer-by-layer analyzes of the kind adopted here, and they are typically validated against measured thermocouple histories or experimentally observed melt-pool dimensions. [31]

2.3.1 Birth and Death Technique

A feature that sets additive-manufacturing simulation apart from conventional finite element analysis is that the workpiece is not present in its final form from the beginning: material is deposited progressively, and the model must represent this growth of the geometry as the analysis proceeds. Meshing the complete part and analyzing it from the outset would allow heat to flow into, and stresses to develop in, regions that have not yet been deposited, which is unphysical. Two main strategies have been developed to avoid this, usually referred to as the quiet-element and the inactive-element methods.

- In the quiet-element method, the elements of the not-yet-deposited material are present in the mesh from the start but are given artificially altered properties — for instance a very low thermal conductivity and heat capacity, or a greatly reduced stiffness — so that they remain essentially inert and do not influence the active part of the model; when a layer is deposited, the true properties of its elements are restored. Its advantage is that the size of the system of equations does not change during the analysis, which simplifies the implementation, but the quiet elements never disappear, so they add to the

computational cost and, if their scaled properties are not chosen carefully, can still introduce small spurious effects such as artificial heat conduction.

- In the inactive-element method, by contrast, the elements of undeposited material are removed from the analysis altogether and are reintroduced only when their layer is laid down, so that they contribute nothing to the equations while inactive. This eliminates the spurious interaction and reduces the active problem size, at the cost of requiring the solver to support the removal and reactivation of elements and a well-defined state for those elements at the instant they are switched on. Comparative studies have shown that the two approaches can give noticeably different results if the quiet-element properties or the reactivation conditions are not handled carefully, and hybrid schemes combining them have also been proposed. [32]

The inactive-element technique — widely known as the element birth-and-death, or element-activation, method — is implemented in Abaqus through the *Model Change command, which deactivates a set of elements with its remove option and reactivates them with add option. [8] An important consideration in any implementation is the state assigned to reactivated material: thermally, the elements should re-enter at the ambient or deposition temperature so that the sensible and latent heat of the fresh material are properly accounted for, and in a coupled analysis they should be reintroduced in a strain-free reference state so that no artificial stress is created. In the present thesis the inactive-element approach is used through *Model Change: the fourteen deposition layers are grouped into separate element sets that are removed at the start of the analysis, leaving only the substrate and the first layer active, and are then reactivated one layer at a time during the successive deposition steps, so that the simulated geometry grows in step with the build.

2.4 Previous Research

Numerical simulation has been widely employed to investigate the thermal behavior, the microstructure evolution and the thermo-mechanical response of additive manufacturing processes. Raghavan et al. [9] developed a three-dimensional transient heat-transfer model of electron-beam melting of IN718 and used it to map the temperature gradient G and the liquid–solid interface velocity R at the trailing edge of the melt pool onto solidification maps; by exploring the influence of beam power, scan speed and preheating they showed how the process window can be adjusted to move the as-built grain morphology between columnar and equiaxed. These numerical predictions are complemented by the combined experimental–

computational study of Knapp et al. [19], who compared simulated melt-pool geometry and solidification parameters for IN718 with single-track experiments and measured dendrite arm spacings, confirming that thermal models of this class can predict the scale of the solidification structure.

Mukherjee et al. [10] used a three-dimensional heat-transfer and fluid-flow model of laser deposition to derive a non-dimensional thermal-strain parameter ε^* from the Buckingham π theorem, and showed that the susceptibility to distortion grows with the peak temperature rise and the heat input per unit length and decreases with the Fourier number and the flexural rigidity of the structure — the same parameter adopted in Section 8.2.2 of this work. In a companion study, Mukherjee et al. [33] proposed quantitative printability indexes — lack of fusion, thermal strain and composition change by selective vaporization — and compared them across common additive-manufacturing alloys, providing the framework followed in the printability analysis of this thesis.

For the tool steel considered here, Bailey et al. [11] developed a self-consistent transient model of multi-track, multi-layer laser direct deposition of H13 that tracks the melt-pool free surface and predicts the temperature history, the solid-state phase transformations, the hardness map and the residual stresses; the predictions were validated against measured cross-sectional hardness distributions and compared with X-ray-diffraction residual-stress measurements on deposited samples. He et al. [12] solved the coupled mass, momentum, energy and solute-transport equations for double-track laser cladding of H13 and showed that convection in the pool controls both the temperature field and the mixing of the added material, underlining the importance of representing melt-pool convection in simpler, conduction-based models. On the experimental side, Joshi et al. [23] combined directed-energy-deposition experiments on H13 with a computational solidification analysis: they extracted the morphology factor G/R and the cooling rate $G \cdot R$ along the build, linked them to the observed cellular/dendritic substructure and the measured microhardness, and reported the G/R range against which the present predictions are compared in Section 8.3.3. Further experimental studies have characterized the graded microstructure and wear behavior of DED H13 walls [24], the tensile and fracture behavior of laser-melted H13 [25], and the part deflection and residual stresses of H13 processed by laser powder-bed fusion [26].

In the field of multi-material and functionally graded deposition, Li et al. [13] built a coupled thermo-mechanical finite element model of functionally graded parts fabricated by DED and validated the predicted temperature histories and distortion against thermocouple and deflection measurements, showing how the property mismatch between dissimilar alloys drives

residual stress. Gan et al. [7] modeled the deposition of IN718 on a carbon-steel substrate with a heat-transfer and fluid-flow model including Marangoni convection, and validated the computed thermal history and the resulting microhardness against experiments, demonstrating that dissimilar Fe–Ni deposition can be predicted quantitatively. Closest to the present work, Ghanavati et al. [14] studied SS316L–IN718 multi-material walls produced by laser DED with a layer-by-layer finite element thermal model and companion experiments: the model predicted the melt-pool dimensions, cooling rates, temperature gradients and solidification rates, the derived printability and morphology indicators were verified against the fabricated walls, and the change of the solidification structure across the dissimilar interface was captured. Their modeling framework is the direct basis of the present simulation.

Finally, the correlation between cooling rate and the scale of the solidification structure that is used in Section 8.3.2 was established experimentally by Zheng et al. [35], who measured secondary dendrite arm spacings in laser-engineered net-shaping deposits over a wide range of cooling rates and reported the power-law constants adopted here.

Building on these numerical and experimental studies, the present work develops a finite element model in Abaqus to study the thermal behavior and printability of an H13–IN718 multi-material DED structure and to evaluate the thermal and solidification characteristics obtained.

3 Materials Used in the Study

3.1 H13 Tool Steel

H13 (AISI H13) is a chromium–molybdenum–vanadium hot-work tool steel, with a nominal composition of approximately 0.4% carbon, 5% chromium, 1.5% molybdenum and 1% vanadium, the balance being iron. [15] It belongs to the chromium hot-work (H-series) group and is air-hardening, which gives it good dimensional stability during heat treatment. Its defining characteristics are high hardenability and high hot hardness — the ability to retain strength at elevated temperature — together with good resistance to thermal fatigue (heat checking), good toughness and ductility, resistance to softening on prolonged heating, and good wear resistance. Because it withstands the repeated heating and cooling and the mechanical loading of hot-working operations, H13 is one of the most widely used tool steels for die-casting dies, hot-forging dies, extrusion tooling and injection moulds. In the present study it serves both as the substrate and as the material of the lower seven deposited layers, and its melting range (solidus ≈ 1315 °C, liquidus ≈ 1454 °C) and temperature-dependent thermal properties are central to the thermal model. [11]

3.2 Inconel 718

Inconel 718 (IN718) is a nickel–chromium-based superalloy, with a nominal composition of about 50–55% nickel and 17–21% chromium, together with roughly 5% niobium, 3% molybdenum and small additions of titanium and aluminium, the balance being iron. [17] It is an age-hardenable alloy that combines high strength with excellent creep and fatigue resistance and good oxidation and corrosion resistance, and it retains these properties from cryogenic temperatures up to about 650–700 °C, above which its strength begins to fall.

It also has good weldability, which makes it one of the more readily processed superalloys and well suited to additive manufacturing. These qualities make IN718 one of the most widely used superalloys, particularly for aero-engine and gas-turbine components such as discs, blades, casings and combustors, as well as for rocket-engine parts and high-temperature fasteners, and it is among the most extensively studied alloys in metal additive manufacturing. [18] In this study it forms the upper seven deposited layers; its relatively low thermal conductivity and its solidification range (solidus ≈1255 °C, liquidus ≈1337 °C) strongly influence the simulated thermal field. [9]

3.3 Multi-Material Configuration

The modeled component in this thesis is a fourteen-layer thin-wall. The substrate and the first seven layers are H13 and the last seven layers are IN718. Each layer has a thickness of 0.8 mm. The motivation to combine the two alloys is functional. The base is a tough, thermal-fatigue resistant hot-work tool steel, whereas the nickel superalloy provides a surface with superior strength, creep resistance and oxidation resistance at high temperature – the kind of graded steel-to-superalloy structure for which directed energy deposition is one of the few viable manufacturing routes. [13] This type of joining of dissimilar metals, however, is demanding, because the two alloys differ markedly in their thermophysical properties – conductivity, specific heat, density and melting range – and in their metallurgical behavior. These differences change the heat flow and melt-pool response as the build crosses the interface, and can cause dilution, formation of brittle intermetallic phases and residual stresses due to thermal expansion mismatch. The present work is dedicated to the thermal aspect of this interaction. The seven-plus-seven configuration was chosen especially to be able to study the change in thermal behavior at the H13-IN718 transition.

3.4 Thermophysical Properties Used in the Model

All of the thermophysical properties required by the thermal analysis — the density, the thermal conductivity and the specific heat of both alloys — were defined as functions of temperature and taken from published data. The latent heat of fusion of each alloy was also included and was applied over its solidus–liquidus interval through the enthalpy method, so that the energy absorbed on melting and released on solidification is captured automatically. A purely conductive model cannot reproduce the heat transport that takes place inside the molten pool, where buoyancy- and surface-tension-driven (Marangoni) flows circulate the liquid and spread heat far more effectively than conduction alone [10]; if the solid-state conductivity were retained in the pool, the model would underestimate this transport and overpredict the peak temperature. To account for it in an averaged way, the thermal conductivity was treated so as to represent melt-pool convection above the solidus.

For H13 the solid-phase conductivity was raised linearly to about three times its solidus value at 3000 K (2727 °C) and held constant above that, following the standard enhancement approach [14]. Although this three-fold enhancement was originally proposed for austenitic stainless steels, its use for H13 is considered acceptable here because the enhancement is a surrogate for melt-pool convection rather than a property of a particular alloy class: models

that resolve the pool fluid flow directly in H13 itself confirm that Marangoni-driven convection, not conduction, controls the heat transport within the pool [11], [12], and the same conclusion was reached for a dissimilar Fe–Ni deposition system [7]. A comparable effective liquid conductivity is likewise embedded in the IN718 dataset adopted below, so the two alloys are treated consistently. For IN718 the temperature-dependent conductivity of [13] was used directly; that dataset already incorporates an effective liquid conductivity of 100 $W \cdot m^{-1} \cdot K^{-1}$ above ~1344 °C, which accounts in the same averaged way for the convective transport within the molten pool. The complete temperature-dependent property data and latent-heat values used for H13 and IN718 are listed in Tables 3.1–3.4.

Table 3.1. *H13 thermal conductivity, with the enhancement above the solidus (1314.85 °C).* [24]

Temperature, °C	k, $mW \cdot mm^{-1} \cdot K^{-1}$
20	17.6
100	17.6
200	23.0
400	25.0
800	29.5
1084	29.8
1200	29.9
1314.85 (solidus)	30.4
1453.85 (liquidus)	36.4
2000	59.9
2727 (≈3000 K)	91.2
6000	91.2

The high-temperature specific-heat values of H13 (658 $J \cdot kg^{-1} \cdot K^{-1}$ for the solid phase and 804 $J \cdot kg^{-1} \cdot K^{-1}$ for the liquid phase) are taken from Bailey et al. [11], who report C_p as constant phase values rather than a continuous function; the latent heat of fusion is applied separately over the solidus–liquidus interval. The apparent step near the solidus therefore reflects the transition between the lower-temperature data of [24] and the phase-based values of [11], and does not represent a physical decrease in heat capacity.

Table 3.2. *H13 density and specific heat.* [24],[11]

T, °C	ρ, $t \cdot mm^{-3}$	C_p, $mJ \cdot t^{-1} \cdot K^{-1}$
20	7.76×10^{-9}	4.59×10^{8}
200	7.65×10^{-9}	5.18×10^{8}
400	7.60×10^{-9}	5.87×10^{8}

T, °C	ρ, t·mm^{-3}	C_p, mJ·t^{-1}·K^{-1}
800	7.20×10^{-9}	8.85×10^{8}
1084	7.13×10^{-9}	8.17×10^{8}
1200	7.11×10^{-9}	8.61×10^{8}
1450	7.00×10^{-9}	6.58×10^{8}
1600	6.90×10^{-9}	8.04×10^{8}

Table 3.3. *IN718 temperature-dependent thermal properties.* [13]

T, °C	k, mW·mm^{-1}·K^{-1}	ρ, t·mm^{-3}	C_p, mJ·t^{-1}·K^{-1}
25	12	8.22×10^{-9}	4.21×10^{8}
227	14	8.12×10^{-9}	4.53×10^{8}
427	17	8.04×10^{-9}	4.81×10^{8}
727	22	7.961×10^{-9}	5.62×10^{8}
927	26	7.875×10^{-9}	6.36×10^{8}
1127	23	7.787×10^{-9}	6.50×10^{8}
1260	20	7.733×10^{-9}	6.52×10^{8}
1344	100	7.579×10^{-9}	6.52×10^{8}
1450	100	7.488×10^{-9}	6.52×10^{8}

Table 3.4. *Latent heat of fusion and solidus/liquidus temperatures.* [9],[11]

Material	Latent heat, mJ·t^{-1}	Solidus, °C	Liquidus, °C
H13	2.72×10^{11}	1314.85	1453.85
IN718	2.27×10^{11}	1254.85	1336.85

4 Finite Element Modeling Methodology

The numerical model was developed in Abaqus/CAE and solved using the Abaqus/standard finite element solver. A transient heat-transfer analysis was performed to model the thermal evolution of the Laser Directed Energy Deposition (L-DED) process throughout the entire build sequence. The computational domain was discretized using the finite element method into a finite number of elements and the governing heat-transfer equations were solved as a function of space and time.

The overall modeling procedure was consistent with the standard finite element workflow of pre-processing, solution and post-processing. In the pre-processing stage, the geometry, analysis steps, material definitions, interactions and thermal loading conditions were prepared in the Abaqus/CAE environment. The resulting finite element model was then exported as an input file and further modified as necessary to introduce functionalities not directly available through the graphical interface. Then, the numerical solution was performed by Abaqus/Standard which solves the discretized heat-transfer equations in each time increment to obtain the transient temperature field. Finally, the results of the simulation were evaluated in Abaqus/Viewer and temperature contours, thermal histories and other important outputs were extracted for analysis. Abaqus is particularly suited for this type of study since it provides powerful transient thermal analysis capabilities and allows user-defined implementations through input-file modifications and external subroutines. [8]

The modeling approach followed in this work was designed to capture the progressive nature of the DED process at a reasonable computational cost. The entire numerical set up was thus realized by a combination of Abaqus/CAE features, manual keyword editing and user subroutine programming. This method offered the necessary flexibility to capture the sequential deposition process and associated thermal phenomena, while being fully embedded within the Abaqus finite element environment. The detailed implementation of the individual modeling components is described in subsequent sections.

5 Governing Equations and Problem Setup

5.1 Heat-transfer equation

The directed energy deposition process is dominated by conductive heat transfer in the solid, with a moving heat input applied by the laser and convective and radiative losses from the free surfaces. The thermal field is therefore obtained by solving the transient heat-conduction equation:

$$\rho(T)\, C_p(T)\, \partial T/\partial t \;=\; \nabla \cdot (\, k(T)\, \nabla T\,) \;+\; Q_v(x,t) \tag{5.1}$$

in which $T(x, t)$ is the temperature, $\rho(T)$ the density, $C_p(T)$ the specific heat, $k(T)$ the thermal conductivity (assumed isotropic, so that k is a scalar), and $Q_v(x,t)$ the volumetric rate of heat generation by the laser. Physically, the equation expresses conservation of energy per unit volume: the left-hand side is the rate at which sensible heat is stored, the divergence term is the net rate of heat gained by conduction, and the source term is the heat supplied by the laser; all three have units of power per unit volume ($W \cdot m^{-3}$). All three material properties are taken as temperature dependent, with the data listed in Section 3.4, and the equation is solved separately in the H13 and IN718 regions of the model, with continuity of temperature and of normal heat flux enforced across the interface by the mesh-conforming connection between the two regions. Two aspects of the process are represented in an averaged way rather than solved directly, both as described in Section 3.4. Fluid motion within the molten pool is not modeled — the analysis contains no fluid-dynamics equations and the geometry is taken to remain rigid for the purpose of computing the temperature field — and its effect on the distribution of heat is instead carried by the temperature-dependent effective conductivity defined there. The latent heat of fusion likewise does not appear as a separate term in the equation above, but is incorporated through the enthalpy method over the solidus–liquidus interval of each alloy. Mechanical effects — distortion, residual stress and thermo-mechanical coupling — lie outside the scope of this thermal analysis and are addressed in the future-work extension.

5.2 Boundary conditions

Heat loss from the workpiece to its surroundings occurs by both convection in the surrounding gas and radiation from the hot surfaces. Rather than apply these as two independent boundary conditions, the model combines them into a single effective surface-film condition,

$$\begin{cases} -k\, \partial T/\partial n \;=\; h_{eff}(T)(\, T \;-\; T_\infty) \\ h_{eff} \;=\; h_{conv} \;+\; \varepsilon\, \sigma(T^2 \;+\; {T_\infty}^2)(T \;+\; T_\infty) \end{cases} \tag{5.2}$$

where $\partial T/\partial n$ is the temperature gradient in the direction of the outward surface normal, h_{conv} is the convective heat-transfer coefficient, ε is the emissivity of the surface, σ = 5.67×10^{-8} W·m^{-2}·K^{-4} is the Stefan–Boltzmann constant, and T_∞= 25 °C is the temperature of the surroundings. The radiative term has been re-cast through the algebraic identity:

$$T^4 - T_\infty{}^4 = (T - T_\infty)(T + T_\infty)(T^2 + T_\infty{}^2) \quad (5.3)$$

so that the entire heat loss is proportional to $(T - T_\infty)$ and the radiation appears as an additional temperature-dependent contribution to the film coefficient. [7] Radiation is therefore not neglected; it is folded into a temperature-dependent effective coefficient. The value of h_{eff} is small near room temperature, where convection dominates, and rises sharply at high temperature as the radiation term grows, so that is essentially an order of magnitude larger near the melting range than it is at ambient. It is supplied to Abaqus as a tabulated function of T through the *Sfilm and *Film Property cards.

This effective film condition is applied to every external surface of the workpiece that is exposed to the surroundings at each instant of the analysis. The set of external surfaces is not fixed: a face that is external before the next layer is deposited becomes internal as soon as that layer is activated, and is replaced by the new external faces of the freshly deposited material. The bottom face of the substrate, which in practice rests on the build plate or fixturing, is treated by the same film condition, so that heat can also leave the model through the substrate base. No additional condition is imposed at the H13–IN718 interface, because the two regions are joined by a continuous mesh and the conservation of temperature and of normal heat flux across the interface is then automatic.

5.3 Initial condition

At the start of the analysis the substrate and the first deposited layer — the only parts of the model that are active at t = 0 — are taken to be in thermal equilibrium with their surroundings, and the corresponding initial condition:

$$\begin{cases} T(x,0) = T_0 \\ T_0 = 25\,°C \end{cases} \quad (5.4)$$

is imposed uniformly throughout the active region. The remaining thirteen layers are inactive at this point and contribute neither degrees of freedom nor stored energy to the solution. As each of these layers is subsequently activated by *Model Change it enters the analysis at the same reference temperature T_0, which represents the powder being delivered to the melt pool at ambient temperature. The molten state of the freshly deposited material is then produced entirely by the laser source acting on it during its deposition step, rather than by an artificially

elevated initial enthalpy, so that the energy balance over each deposition step is determined by the laser input and the surface heat losses alone.

5.4 Laser heat input

The volumetric heat-generation term in the governing equation of Section 5.1 represents the energy delivered by the laser. It is modeled as a moving volumetric heat source of the Goldak double-ellipsoidal type [6], implemented through a DFLUX user subroutine (Section 7.2). A surface flux would place all of the energy on the top face of the layer, whereas in DED the beam, the powder stream, and the melt pool together spread the absorbed energy through a finite depth of material; a volumetric source captures this, and the double-ellipsoidal form additionally reproduces the asymmetry of a moving pool, which is shorter and steeper ahead of the beam than in the elongated trail behind it. The heat is therefore distributed over two quarter-ellipsoids that share the same transverse half-width and depth but differ in length along the scan direction — a shorter leading half ahead of the source center and a longer trailing half behind it — giving the characteristic comet shape (Figure 5.1).

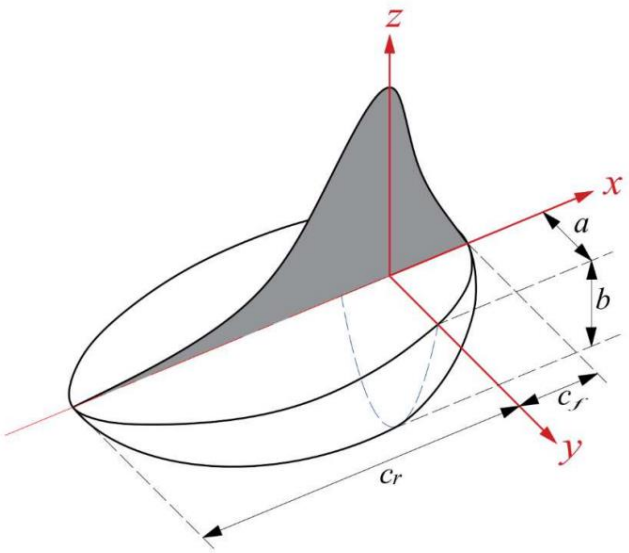

Figure 5.1. *Double-ellipsoidal (Goldak) volumetric heat source representing the laser, with its leading and trailing ellipsoids.* [29]

The redistribution of heat by fluid motion within the molten pool is not represented by the source itself, but is approximated through the above-solidus conductivity enhancement of Section 3.4.

The volumetric flux in the leading (front) and trailing (rear) regions is:

$$q_f = \frac{6\sqrt{3}f_f Q}{abc_f\pi\sqrt{\pi}} \cdot exp[-3(x-x_c)^2/{c_f}^2 - 3(y-y_c)^2/a^2 - 3(z-z_c)^2/b^2] \quad (5.5)$$

$$q_r = \frac{6\sqrt{3} f_r Q}{abc_r \pi\sqrt{\pi}} \cdot exp[-3(x-x_c)^2/{c_r}^2 - 3(y-y_c)^2/a^2 - 3(z-z_c)^2/b^2] \quad (5.6)$$

The quantities a, b, c_f and c_r are the characteristic semi-axes of the Goldak energy distribution — the distances at which the Gaussian flux falls to about 5 % of its peak — and define the volume over which the absorbed power is spread; they are calibration parameters of the heat-source model rather than direct measurements of the melt-pool dimensions. The absorbed power is:

$$Q = \eta P \quad (5.7)$$

the product of the nominal laser power P and an effective absorption efficiency η that lumps together the surface absorptivity and the efficiency with which the blown powder is captured by the pool. The two weighting fractions divide the power between the two halves and satisfy $f_f + f_r = 2$.

The source center advances along the track during each layer's deposition step as:

$$\begin{cases} x_c(t) = x_0 + v(t - t_{to}) \\ y_c = y_0 \\ z_c = z_{sub} + (\text{KSTEP} - 2) \cdot h_L \end{cases} \quad (5.8)$$

with x_0 the start of the track, v the scan speed, y_0 the fixed transverse position of the bead, h_L the layer thickness, and z_{sub} the height of the substrate top. The quantity $t_{to} = t_{Die} + (\text{KSTEP} - 2) \cdot t_{step}$ is the total analysis time at the start of the current layer's step, so subtracting it resets the source to the track start at the beginning of every layer; the center then sweeps across the wall during the scan and runs off the end during the dwell, where the exponential drives the flux to zero and no heat is deposited. The height z_c is raised by one layer thickness each time the step number increases, so the source always sits in the layer currently being built. The laser power and scan speed, together with the calibrated values of the efficiency and the four ellipsoid dimensions, are listed with the subroutine that applies them in Section 7.2 (Table 7.2).

5.5 System of units

Abaqus operates on the numerical values supplied, so all quantities must be expressed in one self-consistent system. A millimetre–tonne–second system was adopted, the natural choice for a geometry given in millimetres. This fixes the derived units: force in newtons, energy in millijoules, and power in milliwatts. Each material and load value taken from the literature in SI units was converted accordingly (Table 5.1). Two conversions are easily missed: thermal conductivity keeps the same numerical value, whereas specific heat and latent heat are

multiplied by 10^6 and the film coefficient by 10^{-3}. The laser power of 250 W becomes 250000 mW and the resulting volumetric flux is in $mW \cdot mm^{-3}$.

Table 5.1. *Consistent millimetre–tonne–second unit system and conversion from SI.*

Quantity	SI unit	mm–t–s unit	SI → mm–t–s
Length	m	mm	$\times 10^3$
Mass	kg	t	$\times 10^{-3}$
Time	s	s	—
Energy	J	mJ	$\times 10^3$
Power	W	mW	$\times 10^3$
Density	$kg \cdot m^{-3}$	$t \cdot mm^{-3}$	$\times 10^{-12}$
Conductivity	$W \cdot m^{-1} \cdot K^{-1}$	$mW \cdot mm^{-1} \cdot K^{-1}$	$\times 1$
Specific heat	$J \cdot kg^{-1} \cdot K^{-1}$	$mJ \cdot t^{-1} \cdot K^{-1}$	$\times 10^6$
Latent heat	$J \cdot kg^{-1}$	$mJ \cdot t^{-1}$	$\times 10^6$
Film coefficient	$W \cdot m^{-2} \cdot K^{-1}$	$mW \cdot mm^{-2} \cdot K^{-1}$	$\times 10^{-3}$

6 Abaqus Modeling Procedure

6.1 Geometry

The substrate and the deposited region were created as three-dimensional solids. The substrate measures 40 mm × 40 mm × 5 mm. The deposited wall is 20 mm long and 0.6 mm wide and consists of fourteen layers, each 0.8 mm thick, giving a total height of 11.2 mm above the substrate. The wall is built along the +Z direction, the laser scans along +X, and Y is the transverse (width) direction. The wall was created as a single part partitioned into fourteen layer-shaped cells, so that adjacent layers share nodes and the interlayer connection is automatically continuous; the substrate is a separate part, and the two were brought together in a single assembly, with the substrate bonded to the underside of the wall by a single tie constraint (Figure 6.1).

So that the individual regions of the model could be referenced throughout the analysis, named sets were defined for them: an element set for each layer and for the substrate (ESet_L01–ESet_L14 and ESet_Substrate), together with the corresponding part-level sets (PSet_L01–PSet_L14 and PSet_Substrate). These sets are used to assign the materials and sections (Section 6.3), to activate the layers one at a time during deposition (Section 7.1.2), and to direct the moving heat source onto the layer currently being written at each step (Section 7.2).

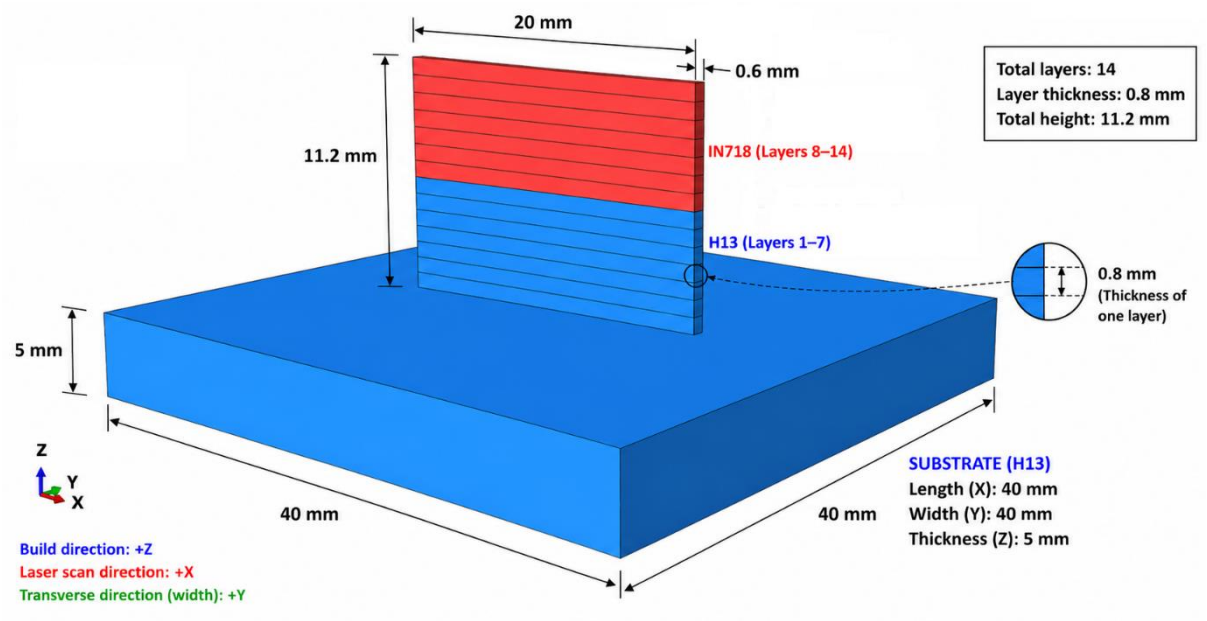

Figure 6.1. *Geometry, showing the H13 substrate, the H13 lower layers, the IN718 upper layers and details.*

6.2 Meshing

The model was discretized with eight-node linear hexahedral heat-transfer elements (Abaqus type DC3D8) [8], a first-order brick element carrying a single temperature degree of freedom at each node. Hexahedral elements were used in preference to tetrahedra because both the substrate and the wall have a regular, prismatic geometry that can be meshed with a structured grid, which gives better accuracy per element and more uniform element quality than an unstructured tetrahedral mesh. A graded mesh was adopted so that the computational effort is concentrated where the thermal gradients are steepest; the parts were seeded accordingly and the mesh then generated.

In the deposited wall, where the moving melt pool produces very sharp gradients in both space and time, a fine seed size of 0.2 mm was applied in all three directions (Figure 6.3). This places four elements through the thickness of each 0.8 mm layer — sufficient to resolve the through-thickness temperature gradient and the size of the melt pool — and gives one hundred elements along the 20 mm scan length and three across the 0.6 mm width of the wall. Each layer therefore contains 1200 elements (100 × 3 × 4), and the fourteen-layer wall contains 16800 elements in total. The substrate, in which the gradients are much milder away from the deposition zone, was seeded more coarsely at 1 mm to keep the model size manageable; with its 40 × 40 × 5 mm dimensions this gives 8000 elements (Figure 6.2). The complete model therefore comprises 24800 elements (Figure 6.4).

Because the fine mesh of the wall and the coarse mesh of the substrate do not share coincident nodes on their common surface, the two regions are joined by a tie constraint. The deposit (wall) surface is defined as the master surface and the substrate surface as the slave surface. The tie enforces continuity of both temperature and heat flux across the wall–substrate interface, so that heat is conducted from the hotter deposited material into the substrate without requiring conformal meshes at the interface.

A refinement of this discretization would be to grade the substrate mesh so that it is finer adjacent to the wall — where the substrate gradients are steepest — and coarsens toward the plate edges; the uniform 1 mm substrate seed was retained here for simplicity, and this local grading is noted as an improvement for future models.

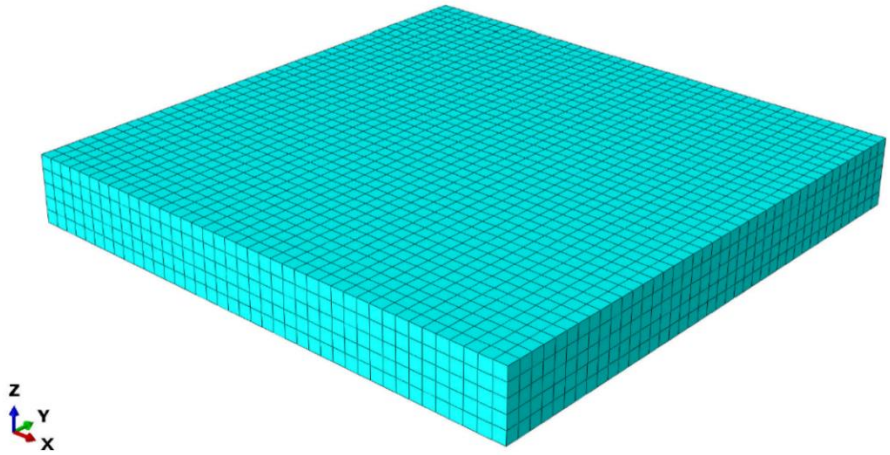

Figure 6.2. *Finite-element mesh of the substrate.*

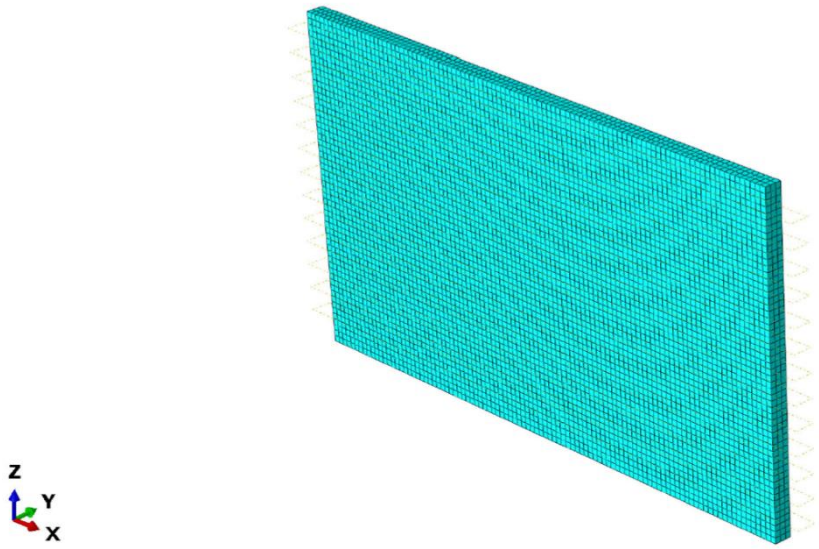

Figure 6.3. *Detail of the graded mesh in the deposited wall.*

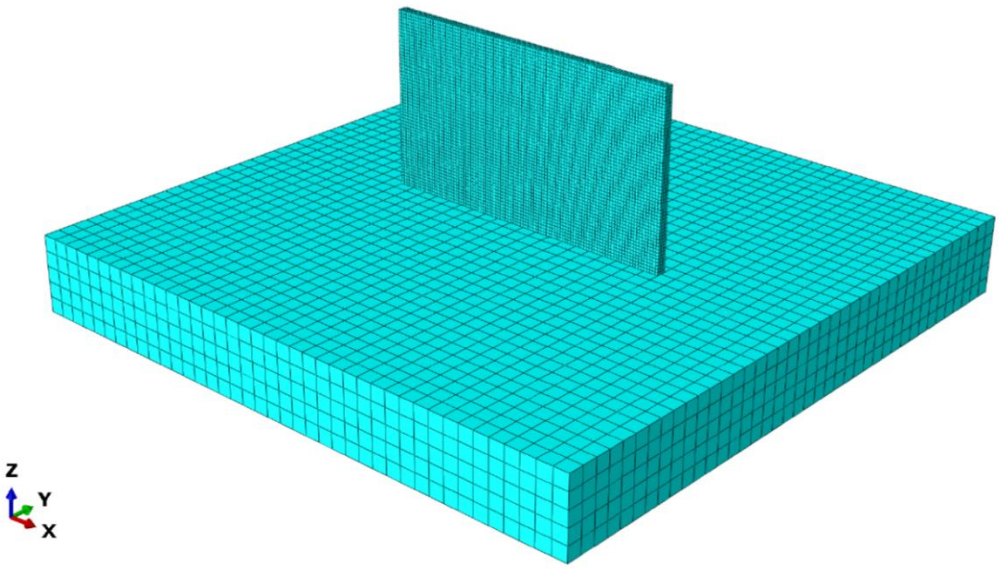

Figure 6.4. *Finite-element mesh of the substrate and the deposited wall.*

6.3 Material definition

Two materials, H13 and IN718, were defined in the model. For each alloy the density, specific heat and thermal conductivity were entered as tabulated functions of temperature, and the latent heat of fusion was specified together with the solidus and liquidus temperatures of that alloy. The complete property data, including the above-solidus conductivity enhancement and the treatment of the latent heat, are given in Section 3.4.

The materials were applied to the geometry through section assignments: a solid section was created for each alloy and assigned using the element sets of Section 6.1, with H13 given to the substrate and the lower seven deposited layers and IN718 to the upper seven layers, reproducing the seven-plus-seven configuration described in Section 3.3.

6.4 Steps

The initial temperature (Section 5.3) is imposed as a predefined field before the analysis begins. The analysis itself is carried out in sixteen steps — a Die step, fourteen deposition steps (D1–D14) and a final Cooling step — each of which is a transient heat-transfer step.

The Die step comes first and applies no heating; its role is to set up the model before any material is deposited. Through the element birth-and-death scheme (Section 7.1.2) it deactivates the thirteen upper layers that have not yet been built, leaving only the substrate and the first layer active, and it establishes the surface-film condition (Sections 5.2–5.3) on the exposed surfaces together with the moving heat source that is applied during deposition.

Each of the fourteen D steps then deposits one layer: the layer is brought into the model (Section 7.1.2) and the moving laser source travels along it, so that the step spans both the scanning time and the dwell time that follows before the next layer is deposited.

The final Cooling step carries no heat input and is longer than the individual deposition steps; once the laser has been switched off, it allows the completed wall and substrate to cool back towards the ambient temperature.

All sixteen steps are transient because the temperature field evolves continuously in time: the heat source moves during deposition, and the material continually stores and releases heat through its thermal capacitance (the $\rho c \cdot \partial T/\partial t$ term). A steady-state analysis, which assumes $\partial T/\partial t = 0$, could not capture this behavior.

7 Codes and INP Modifications

After the model had been built in Abaqus/CAE (Chapter 6), it was written to an input (.inp) file and then edited by hand, because two features of the analysis cannot be produced through the CAE interface: the layer-by-layer activation of the deposited material, and the moving Goldak heat source. The activation was added with *Model Change keywords, the heat source with *Dflux keywords, and the value of the moving flux is computed by a Fortran user subroutine (DFLUX). This chapter presents and explains those additions.

7.1 Modifications to the Abaqus input file

7.1.1 Step structure

Each of the analysis steps (Section 6.4) is defined in the input file as a transient heat-transfer step. A typical step, deposition step D1, is written as:

```
*Step, name=D1, nlgeom=NO, inc=10000000
*Heat Transfer, end=PERIOD, deltmx=100.
0.001, 24., 1e-10, 24.
```

- On the *Step line, nlgeom=NO indicates that geometric nonlinearity is not considered: the analysis is purely thermal, so no deformation is computed and the large-displacement formulation is unnecessary.
- inc=10000000 raises the limit on the number of increments the step may use; the default limit is small, and because the moving source forces a great many short increments (explained below), the cap is set high so that the solver is never halted before the step has finished.
- The *Heat Transfer keyword requests a thermal solution, and end=PERIOD makes that solution transient and run for the full specified time period, rather than stopping early as soon as a steady state is detected.
- deltmx=100. limits the temperature change permitted at any node within a single increment to 100 °C. Abaqus uses this to drive automatic (adaptive) time incrementation: it chooses the size of each increment so that the limit is respected, taking very small increments while the melt pool is sweeping across the layer and the local temperature is changing by hundreds of degrees, and much larger increments during the quiet interlayer dwell, when the temperatures change only slowly. A smaller deltmx therefore buys a finer, more accurate resolution of the moving pool and the steep

gradients around it, at the cost of more increments and a longer run; the value of 100 °C was used for the final analysis to give clean melt-pool peaks.

- The four numbers on the data line are the initial time increment, the total step time (the period), and the minimum and maximum allowable increments. For this step the solver starts from a 0.001 s increment, may shrink it as far as 1×10^{-10} s if convergence requires, and may grow it up to the full 24 s, always within the deltmx limit. The 24 s period is itself made up of a 4 s scan — the 20 mm track travelled at 5 mm·s^{-1} — followed by a 20 s interlayer dwell, during which the laser has run off the end of the track and the layer cools before the next one is deposited.

The deposition steps D1–D13 each use this 24 s period; D14 lasts only 4 s, because the final layer is not followed by a dwell; the Die step is a single second; and the Cooling step runs for 1800 s (thirty minutes) to bring the completed wall back down towards ambient. The total simulated process time is therefore 2117 s.

7.1.2 Element activation (birth and death)

The inactive-element scheme described in Section 2.3.1 is realized in this model through the *Model Change command. The deposited wall is partitioned so that each of its fourteen layers forms its own element set, ESet_L01–ESet_L14 (Section 6.1); the substrate is held in a separate set that is never removed, since it represents the existing baseplate rather than deposited material. In the Die step the upper thirteen-layer sets are removed, leaving only the substrate and the first layer active:

```
** Interaction: Remove-inactive-layers
*Model Change, remove
ESet_L02
ESet_L03
ESet_L04
ESet_L05
ESet_L06
ESet_L07
ESet_L08
ESet_L09
ESet_L10
ESet_L11
ESet_L12
ESet_L13
ESet_L14
```

The remove option deactivates these elements until their layer is deposited: while inactive they take no part in the solution, their faces carry no surface film, and they are not drawn in the results. The first layer is deliberately left active, so that it is present from the outset and is simply melted by the laser during step D1.

One layer is then reactivated at the start of each deposition step with the add option. Step D2, for example, restores layer 2:

```
** Interaction: Activate-L02
*Model Change, add
ESet_L02
```

D3 adds ESet_L03, and so on up to D14, which adds ESet_L14.

Because the wall was meshed as a single partitioned solid rather than as a stack of separate parts, the layers share nodes across their common faces. A reactivated layer is therefore connected to the one beneath it the instant it is added, with no tie or contact pair required between layers. The shared nodes also mean that each interface is treated as perfectly bonded thermally, with no interfacial contact resistance from one layer to the next — a reasonable idealization for fully fused deposited material, though one that will tend to make the through-thickness heat flow slightly more efficient than in reality.

The state in which a layer re-enters the analysis follows the reasoning of Section 2.3.1. Because the upper layers are removed in the Die step while the whole model is still at its initial temperature, each layer re-enters at that ambient temperature (Section 5.3) when it is reactivated, representing cold feedstock that is only then brought to the melt by the laser. As the present analysis is purely thermal, this re-entry temperature is the only reactivation state that matters; the strain-free reference state mentioned in Section 2.3.1 would become relevant only if these thermal results were later carried into a coupled stress analysis.

The full sequence of steps, and the layer activated in each, is given in Table 7.1.

Table 7.1. *Analysis-step sequence and the layer activated in each step. KSTEP is the index passed to the DFLUX subroutine.*

Step	KSTEP	Layer added	Material	Heat source
Die	1	— (removes L2–L14)	—	off
D1	2	1	H13	on
…	…	…	…	…
D7	8	7	H13	on
D8	9	8	IN718	on
…	…	…	…	…
D14	15	14	IN718	on
Cooling	16	— (cool-down)	—	off

7.1.3 Moving heat source

The moving Goldak source of Section 5.4 is defined in the input file as a non-uniform distributed body flux. The *Dflux keyword is written once, in the Die step, and applied to all fourteen-layer sets:

```
** Name: Load-1   Type: Body heat flux
*Dflux
ESet_L01, BFNU, 1.
ESet_L02, BFNU, 1.
...
ESet_L14, BFNU, 1.
```

BFNU is the load type "body flux, non-uniform." A uniform body flux would take the constant value written on the data line, but for a non-uniform flux Abaqus ignores that value and instead obtains the flux from the DFLUX user subroutine (Section 7.2), calling it at every integration point of these elements on every increment. The trailing 1. is therefore only a reference magnitude, left at unity so that the value returned by the subroutine is applied as it stands. Declaring the load on all fourteen sets makes every layer ready to receive the flux the moment it is activated; while a layer is inactive, or active but not currently under the source, the subroutine returns zero and no heat is applied. Because the load is defined in the Die step it propagates automatically to all of the deposition steps that follow. For the final cool-down it is switched off in the Cooling step by re-issuing the keyword with the op=NEW parameter and no data lines, which replaces the earlier definition with an empty one:

```
*Dflux, op=NEW
```

7.1.4 Surface heat loss and initial temperature

Heat loss from the exposed surfaces is applied with the *Sfilm keyword on the external surface of the model:

```
** Interaction: Film
*Sfilm
All_External_Surf, F, 25., IntProp-1
```

- All_External_Surf is the surface set exposed to the surroundings,
- *F* denotes a film (convective-type) condition,
- 25. is the sink (ambient) temperature in °C.
- IntProp-1, is the name of a temperature-dependent film property rather than a constant: at each temperature it supplies the effective coefficient that combines convection and radiation into a single value, as derived in Section 5.2. Applying the condition over the

whole external surface means each layer loses heat to the surroundings as soon as its faces are exposed by the deposition sequence.

The starting temperature of the whole model is set in the model-data section, before the steps:

```
*Initial Conditions, type=TEMPERATURE
Nall, 25.
```

This assigns 25 °C to every node (Nall) at the start of the analysis. It is also the temperature at which the upper layers re-enter the model when they are reactivated (Section 7.1.2), so the single statement fixes both the initial state of the substrate and first layer and the temperature of each fresh layer as it is added.

7.2 The Goldak DFLUX user subroutine

The value supplied by the BFNU load is computed by the DFLUX subroutine, which evaluates the Goldak source of Section 5.4 at each integration point. At each call Abaqus passes it the step and increment numbers (KSTEP, KINC), the total analysis time (TIME(2)), and the coordinates of the point (COORDS); the subroutine returns the volumetric flux FLUX(1) at that point, in the model units of $mW \cdot mm^{-3}$.

The heat-source model contains an effective absorption efficiency η that lumps together the surface absorptivity of the material and the fraction of the blown powder captured by the pool. Such an efficiency cannot be measured directly and is obtained by trial-and-error calibration, the criterion being that the computed layer peak temperatures fall within the physically expected range for laser DED — above the liquidus of the alloy being deposited but below its boiling range, and consistent with the peak temperatures reported for laser-deposited IN718 [7].

Because H13 and IN718 are both metal powders with similar absorptivity, a single material-independent value $\eta = 0.30$ is used for the bulk of the build (layers 2–13), and no change of efficiency is imposed at the H13-to-IN718 material transition. Two exceptions are made that depend on the position of the layer rather than on its material: the first layer, deposited onto the cold machined substrate, requires a higher value ($\eta = 0.45$) for the pool to form and wet the substrate, and the final layer, which is not followed by an interlayer dwell, uses a slightly reduced value ($\eta = 0.27$) to avoid an artificial overshoot of the last peak.

Table 7.2. *Heat-source and process parameters (final calibrated values).*

Parameter	Symbol	Value	Unit
Laser power	P	250 000	mW
Scan speed	v	5	mm·s^{-1}
Layer thickness	h_L	0.8	mm
Efficiency (layers 2–13)	η_{bulk}	0.30	—
Efficiency (layer 1)	η_{L1}	0.45	—
Efficiency (layer 14)	η_{L14}	0.27	—
Transverse half-width	a	0.55	mm
Penetration depth	b	1.60	mm
Front / rear length	c_f / c_r	0.40/0.55	mm
Front / rear fractions	f_f / f_r	1.0/1.0	—

The laser power and scan speed, and the calibrated efficiency and ellipsoid dimensions it uses, are those of the heat-source model of Section 5.4, collected in Table 7.2. The penetration depth b = 1.6 mm corresponds to the lower bound of the 1.6–2.5 mm range used for the same double-ellipsoidal source in the reference calibration of Ghanavati et al. [14]; together with the 0.8 mm layer thickness, it sets the one-to-a-few-layer remelting depth that the source must reproduce.

```
      SUBROUTINE DFLUX(FLUX,SOL,KSTEP,KINC,TIME,NOEL,NPT,COORDS,
     1 JLTYP,TEMP,PRESS,SNAME)
      INCLUDE 'ABA_PARAM.INC'
      DIMENSION FLUX(2), TIME(2), COORDS(3)
      CHARACTER*80 SNAME
      REAL*8 T, etta, P, Q, b, a, ff, fr, cr, cf
      REAL*8 V, Pi, Q0, tto
      REAL*8 x0, y0, z0_layer
      REAL*8 xc, yc
      REAL*8 x, y, z, val

      FLUX(1) = 0.0D0
      FLUX(2) = 0.0D0
C  MODEL UNITS:  mm - tonne - s - degC      flux -> mW/mm^3
      T   = TIME(2)
      Pi  = 3.141592653D0
      V   = 5.0D0          ! scan speed  (mm/s)
      x0  = 10.0D0         ! scan start  x  (mm)
      y0  = 10.0D0         ! track center y (mm)
      x = COORDS(1)
      y = COORDS(2)
      z = COORDS(3)
C  STEP FILTER : laser only fires during D1..D14
C  Die=KSTEP 1, D1=KSTEP 2 ... D14=KSTEP 15, Cooling=KSTEP 16
      IF (KSTEP .LT. 2 .OR. KSTEP .GT. 15) RETURN
C  LAYER N = KSTEP-1 ; tto = step start time ; z0 = layer bottom
      tto      = 1.0D0 + DBLE(KSTEP-2)*24.0D0
      z0_layer = 5.0D0 + DBLE(KSTEP-2)*0.8D0
C  LASER POSITION  (scan = +X, advances within the step)
      xc = x0 + V*(T - tto)
      yc = y0
C  ============================================================
C  EFFECTIVE EFFICIENCY (CALIBRATION KNOB)
C  Single material-independent value: H13 and IN718 are powders
```

```
C  of similar absorptivity, so eta is NOT switched on material.
C  eta = 0.30 was already validated, mid-build peaks ~2100-2180 degC, consistent
C  with Gan et al. for laser-deposited IN718).
C  Positional exceptions (allowed: first / last layer only):
C    Layer 1  (KSTEP  2): eta = 0.45 - cold machined substrate;
C                         at 0.30 the layer would not melt.
C    Layer 14 (KSTEP 15): eta = 0.27 - no interlayer dwell
C                         follows; trimmed to avoid overshoot.
C  ================================================================
      P = 250000.D0        ! laser power 250 W  (-> mW)
      IF (KSTEP .EQ. 2) THEN
        etta = 0.45D0      ! layer 1  (first-layer exception)
      ELSE IF (KSTEP .EQ. 15) THEN
        etta = 0.27D0      ! layer 14 (last-layer exception)
      ELSE
        etta = 0.30D0      ! layers 2-13 (single bulk value)
      END IF
      Q  = etta * P
C  GOLDAK ELLIPSOID PARAMETERS  (mm)
      a  = 0.55D0
      b  = 1.60D0
      cf = 0.40D0
      cr = 0.55D0
      ff = 1.0D0
      fr = 1.0D0
      Q0 = (Q*6.D0*(3.D0**0.5D0)) / ((a*b)*(Pi**1.5D0))
C  DOUBLE ELLIPSOID  (front/rear split on scan axis X)
      IF (x .LE. xc) THEN
        val = (x-xc)**2/(cr**2)
     &      + (y-yc)**2/(a**2)
     &      + (z-z0_layer)**2/(b**2)
        IF (val .LT. 1.0D0) THEN
          FLUX(1) = Q0*(fr/cr)*EXP(-3.0D0*val)
        END IF
      ELSE
        val = (x-xc)**2/(cf**2)
     &      + (y-yc)**2/(a**2)
     &      + (z-z0_layer)**2/(b**2)
        IF (val .LT. 1.0D0) THEN
          FLUX(1) = Q0*(ff/cf)*EXP(-3.0D0*val)
        END IF
      END IF

      RETURN
      END
```

The subroutine carries out the same sequence at every call, for each integration point of each active element:

1. **Initialization.** Both components of the flux array are set to zero. FLUX(1) is the volumetric heat flux returned to Abaqus, in $mW \cdot mm^{-3}$; FLUX(2) is the optional derivative of that flux with respect to temperature, which the solver can use to speed convergence. It is left at zero, and the estimated local temperature SOL that Abaqus also passes is not used, because the Goldak source depends only on position and time and not on the evolving thermal field. The current analysis time and the coordinates of the integration point are then read, and all arithmetic is carried out in double precision, since the exponential in the source is sensitive to small differences in the squared distances.

2. **Step filter.** The test IF (KSTEP .LT. 2 .OR. KSTEP .GT. 15) RETURN allows the source to act only during the fourteen deposition steps (KSTEP 2–15); in the Die step (KSTEP 1) and the Cooling step (KSTEP 16) the routine returns immediately with zero flux, so no heat is applied before deposition begins or after it ends. The increment number KINC is also passed but is not used, since the source is a continuous function of time and position rather than of the increment count.
3. **Layer and position.** From the step number the routine forms the current layer index N = KSTEP − 1, the time origin at which the step began, and the height of the bottom of the current layer, and it computes the instantaneous position of the source center along the track — all as defined for the model in Section 5.4. Resetting the time origin at each step returns the source to the start of the track for every new layer, and raising by one layer thickness each step keeps it centered on the layer currently being built.
4. **Layer-dependent power.** A single absorption efficiency is used for both alloys: every deposition step takes the bulk value, and only the first layer (KSTEP = 2) and the last layer (KSTEP = 15) receive their positional values, after which the absorbed power $Q = \eta \cdot P$ is formed. The two materials are therefore not distinguished inside the source, and no step change in heat input is imposed at the H13–IN718 interface; any difference that appears there in the results arises from the alloy properties alone.
5. **Front/rear selection.** The part of the Goldak pre-factor common to both halves is computed once and stored in Q_0. Each integration point is then assigned to one of the two half-ellipsoids: to the rear (trailing) half, using the rear length c_r, if it lies behind the moving center ($x \leq x_c$), and to the shorter front (leading) half, using c_f, otherwise. This is how the elongated trailing pool and the steep leading edge of the comet shape introduced in Section 5.4 are produced in the code.
6. **Ellipsoid test and flux.** The dimensionless quantity:

$$val = \frac{(x-x_c)^2}{c^2} + \frac{(y-y_c)^2}{a^2} + \frac{(z-z_0)^2}{b^2} \tag{7.1}$$

(with c equal to c_r or c_f according to the half just selected) is the equation of the ellipsoid surface: val < 1 inside, val = 1 on the surface, and val > 1 outside. Only points with val < 1 receive a flux, FLUX(1) = $Q_0 \cdot (f/c) \cdot \exp(-3 \cdot val)$; for every other point the flux stays zero. The test therefore confines the heat to a finite ellipsoidal volume and discards the small Gaussian tail beyond the surface (about five per cent of the peak, as noted in Section 5.4), so the heated region is bounded and well defined rather than extending indefinitely.

Because the flux is applied only within the ellipsoid surface (val < 1), the volume-integrated energy actually deposited is about 89 % of the value implied by the Goldak normalization (the discarded Gaussian tail beyond val = 1 carries roughly 11 % of the integral, even though the flux there has already fallen to ~5 % of its peak). This truncation is absorbed into the calibrated efficiency η, which is therefore an effective coefficient: η was tuned so that the deposited energy reproduces the target melt-pool response, so the net energy input to the part is consistent with the calibration despite the truncation.

7. **Penetration into earlier layers.** Because the source has a finite penetration depth b, the ellipsoid generally reaches below the layer being scanned, so the routine also deposits energy in the previously deposited material that lies within that depth. This is the mechanism that remelts the underlying layer and forms the metallurgical bond later quantified through the melt-pool depth in Section 8.2.1. Layers that have not yet been activated take no part in the solution and the subroutine is never evaluated for them (Section 7.1.2), so an integration point receives heat only once its layer is active and only while the moving ellipsoid of the current step passes over it.

8 Results and Discussion

This chapter presents and discusses the results obtained from the model described in the preceding chapters. The discussion proceeds from the temperature field and the melt pool to the build-up of heat through the deposition sequence, the cooling behavior, the influence of the H13-to-IN718 material transition, the role of the above-solidus conductivity enhancement, and the numerical behavior of the solution. These results sections report both the direct thermal output and the quantities derived from it by post-processing — lack of fusion, thermal strain, and composition change as printability indexes, as well as cooling behavior and solidification structure characteristics (size and morphology). Unless stated otherwise, temperatures are nodal temperatures (the NT11 output) in degrees Celsius, and all contour plots are taken directly from the simulation output.

8.1 Thermal behavior

8.1.1 Temperature distribution and melt pool

The simulation resulted in a transient temperature field during the deposition process. As expected for a concentrated moving heat source the highest temperatures were observed in the material directly beneath the laser and the melt pool developed the characteristic elongated comet shape; a short steep leading edge ahead of the source and a longer trailing region behind the source reflecting the front and rear geometry of the double-ellipsoidal Goldak heat source model [6]. Significant thermal gradients were found between the active deposition zone, the previously deposited material and the substrate, whereas the surrounding regions were at significantly lower temperatures.

The maximum temperatures obtained during the scan of each layer were extracted directly from the simulation results. The peak temperature reached in each deposited layer during the deposition process ranged from 1822 – 2472 °C in the H13 region and 2110 – 2397 °C in the IN718 region. For all deposited layers, the recorded temperatures were higher than the liquidus temperatures of the respective materials (~1454 °C for H13 and ~1337 °C for IN718), indicating sufficient melting conditions for the formation of the melt pool. However, in the first two deposited layers (D1 and D2), which solidify against the cold substrate, the peak temperature was below the liquidus during the first stage of scanning, indicating that the melt pool was not stable from the beginning of the pass but became established only as the laser advanced along the track.

Table 8.1 below shows the shape of the melt pool at a representative node indicative of the melt pool formed within that layer and the range of peak temperature experienced during deposition for each layer. Moreover, the corresponding area of the melt pool is indicated by the grey colored area in each image. Moving up the table, the melt pool becomes progressively larger — longer along the scan direction and deeper into the underlying layers — because the heat accumulated in the wall (Section 8.1.2) pre-heats the base on which each new layer is deposited, so the same heat input melts a larger volume; the depth and length values are analyzed quantitatively in Section 8.2.1.

Table 8.1. *Peak temperature range and melt-pool extent for each deposited layer.*

Layer	Thermal Contour
Layer1 (D1) H13 Peak temperature range: 1398 – 1822 °C	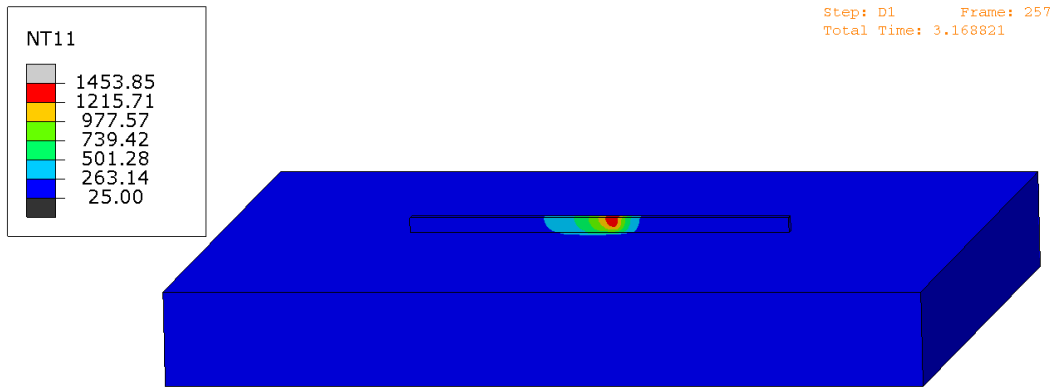
Layer2 (D2) H13 Peak temperature range: 1376 – 1962 °C	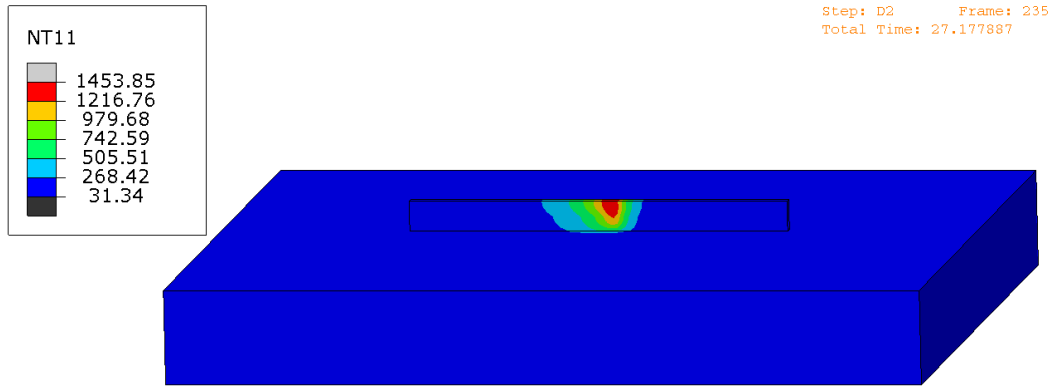
Layer3 (D3) H13 Peak temperature range: 1630 – 2306 °C	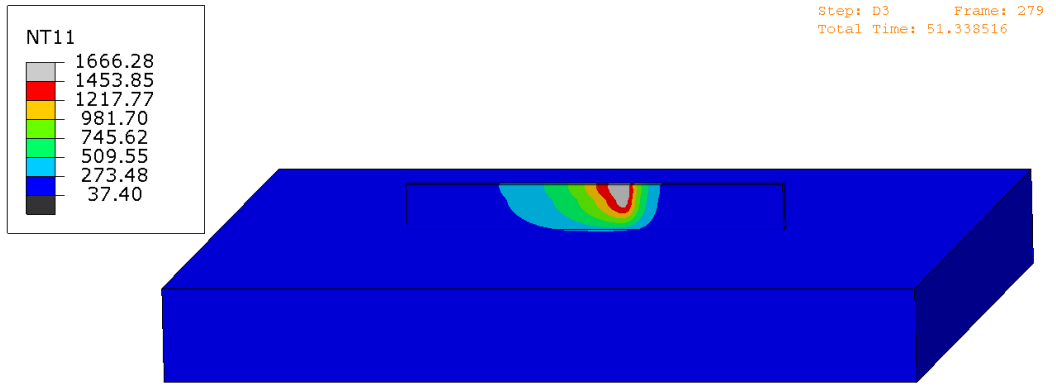

Layer4 (D4) H13 Peak temperature range: 1677 – 2420 °C	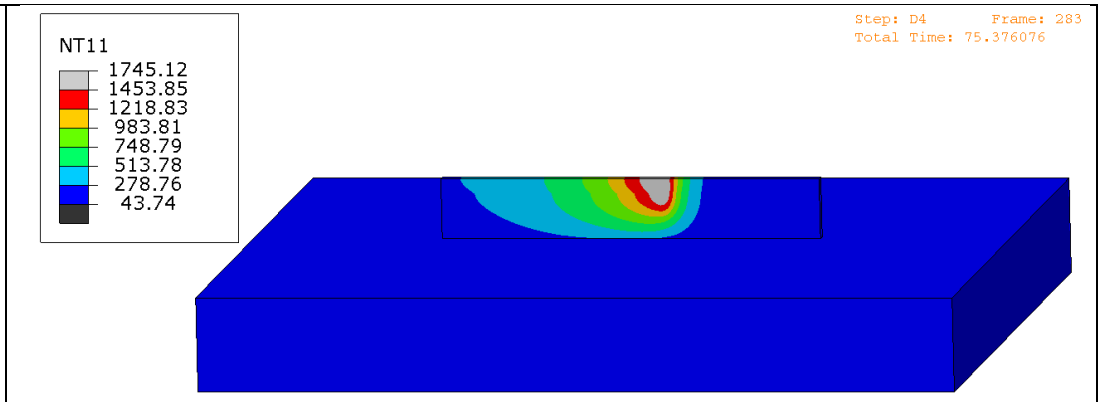
Layer5 (D5) H13 Peak temperature range: 1688 – 2454 °C	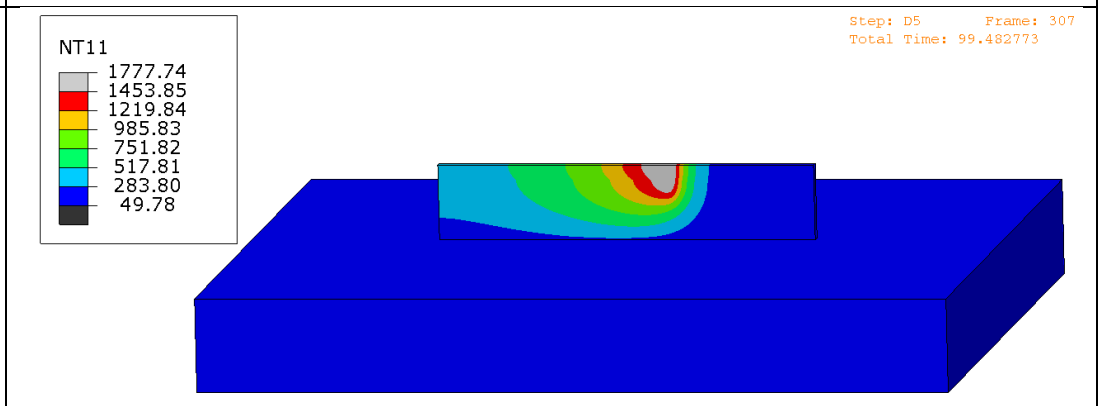
Layer6 (D6) H13 Peak temperature range: 1700 – 2464 °C	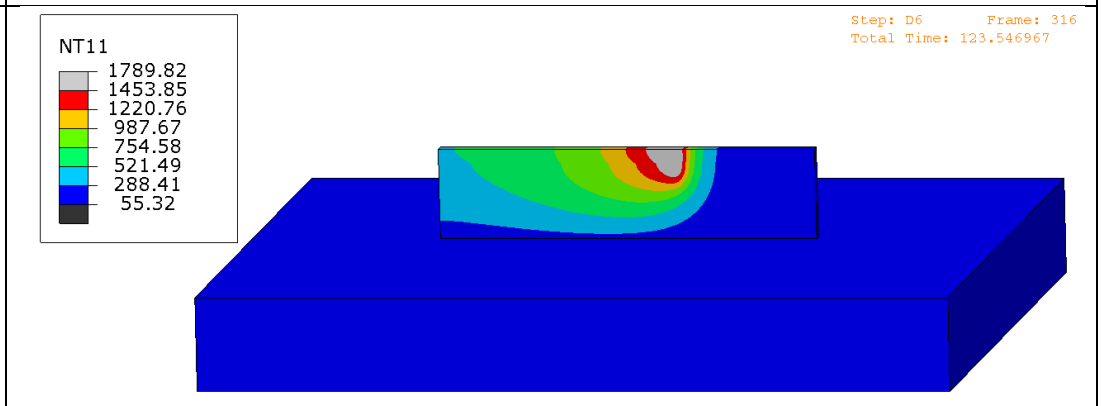
Layer7 (D7) H13 Peak temperature range: 1699 – 2472 °C	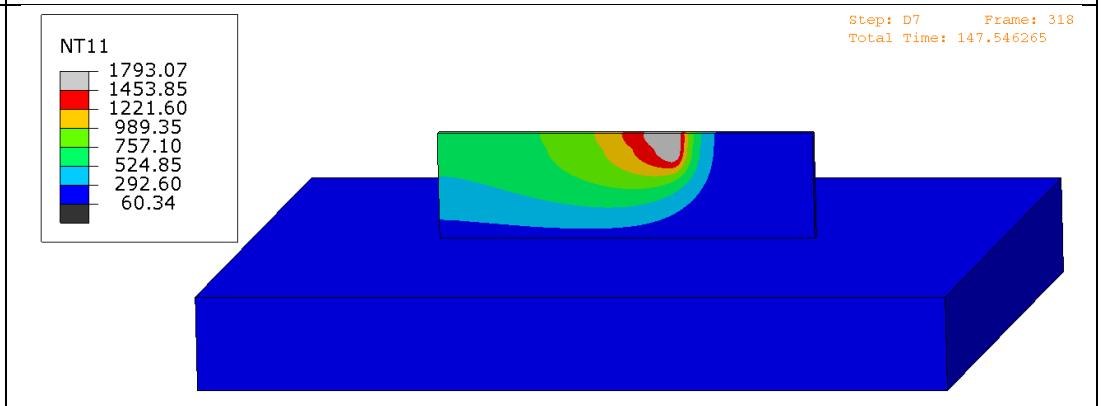

Layer8 (D8) IN718 Peak temperature range: 1647 – 2397 °C	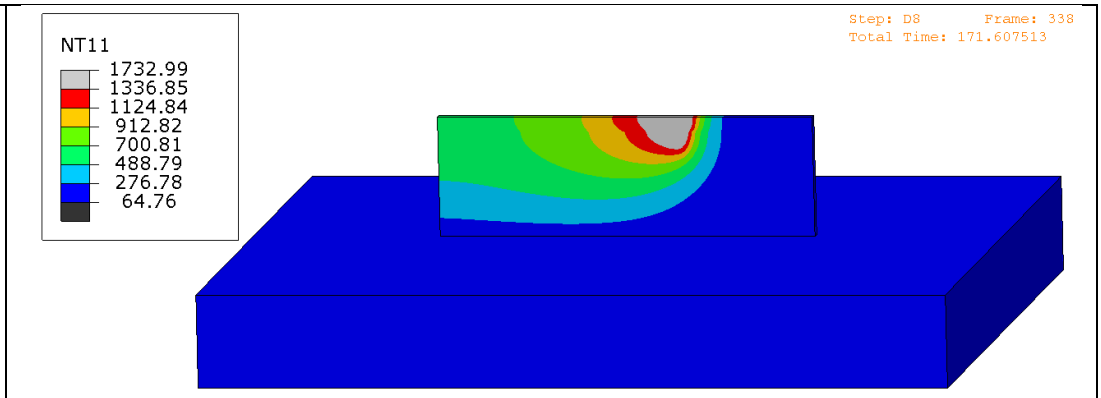
Layer9 (D9) IN718 Peak temperature range: 1526 – 2250 °C	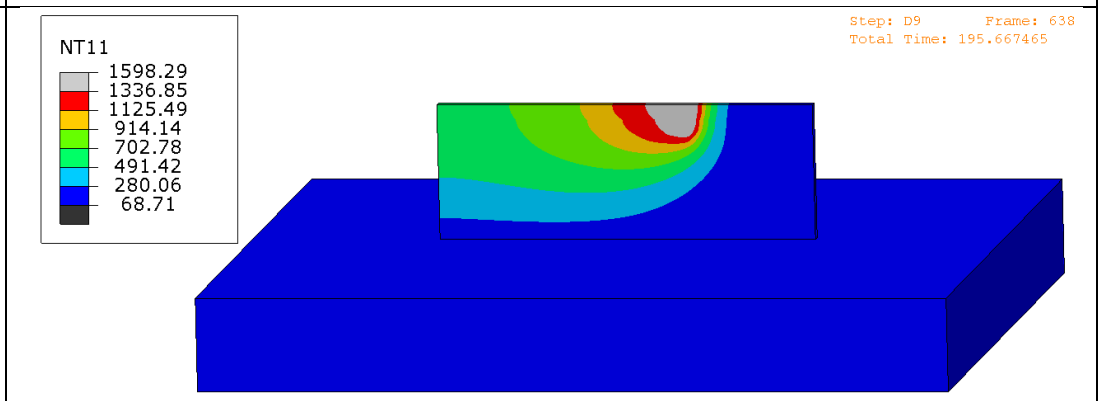
Layer10 (D10) IN718 Peak temperature range: 1539 – 2110 °C	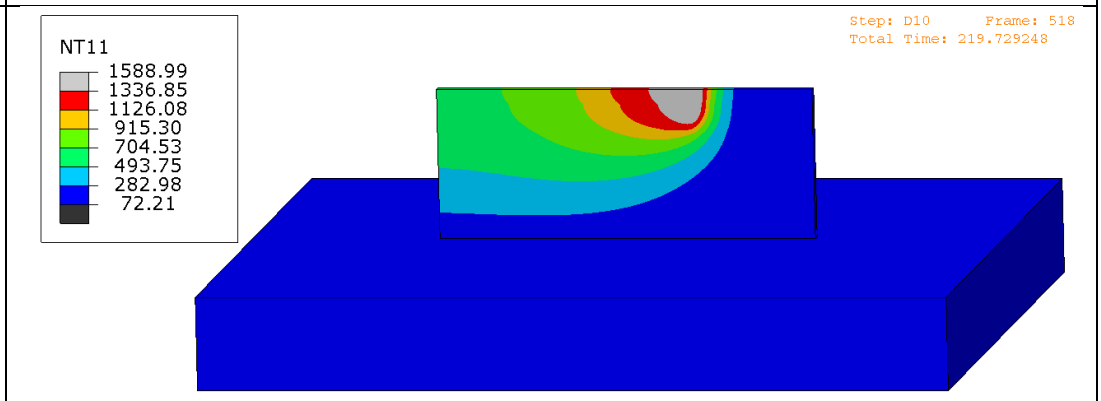
Layer11 (D11) IN718 Peak temperature range: 1546 – 2175 °C	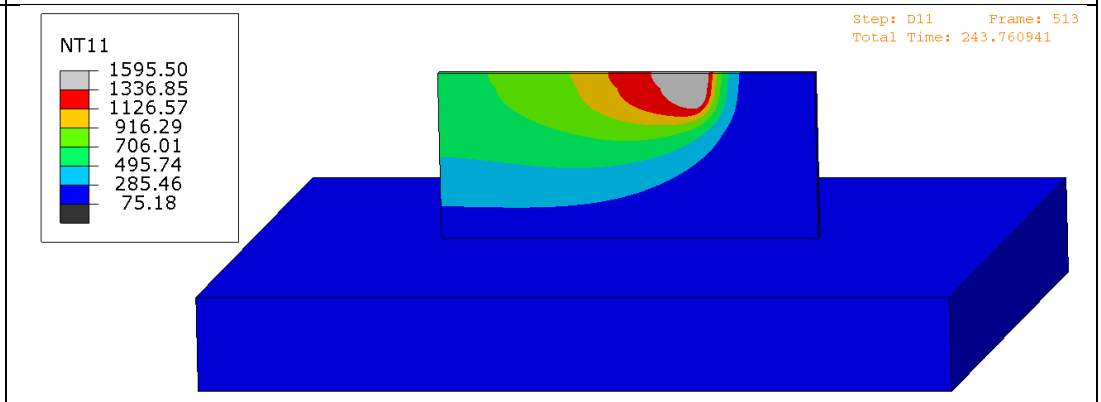

Layer12 (D12) IN718 Peak temperature range: 1550 – 2182 °C	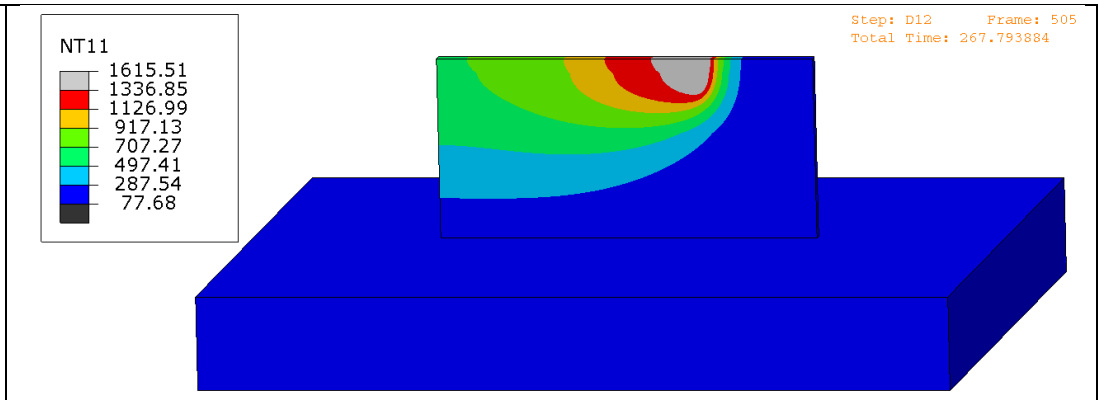
Layer13 (D13) IN718 Peak temperature range: 1553 – 2178 °C	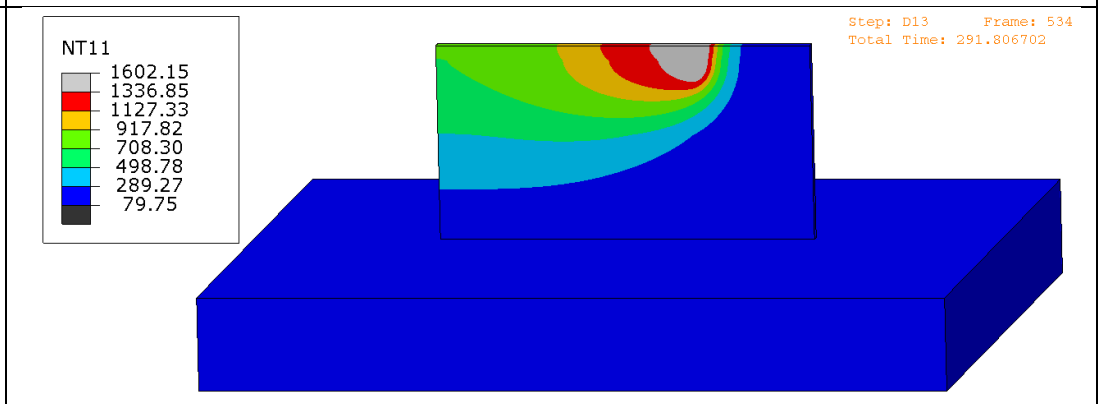
Layer14 (D14) IN718 Peak temperature range: 1506 – 2295 °C	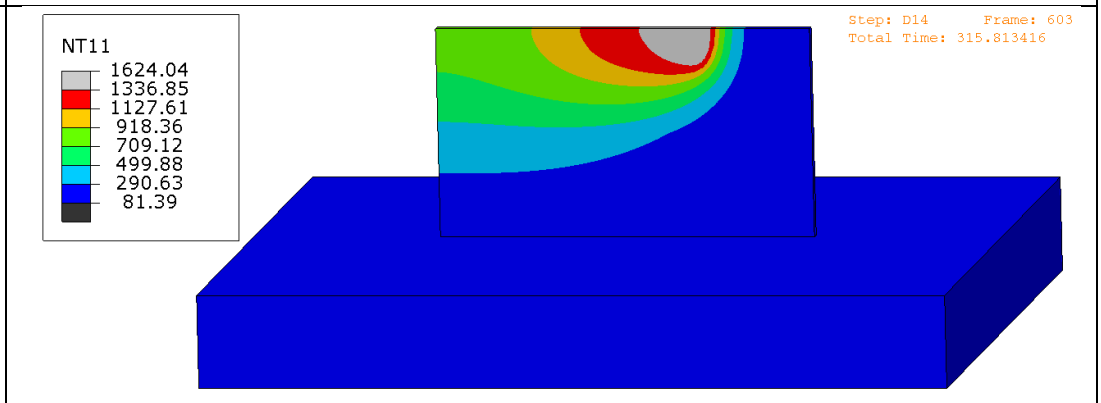

8.1.2 Thermal Evolution and Effect of Material Transition

During deposition the accumulation of heat in the part became more and more important. We can see this in the peak temperatures of the successive layers (Figure 8.1). The first layer peaked at only around 1822 °C. As the wall grew, the layer peaks rose steadily, reaching about 2420–2470 °C in the upper half of the H13 build. This trend is the consequence of three effects. First, as the wall height increases, the conduction path from the deposition zone to the substrate heat sink becomes longer, so heat is less efficiently removed from the upper layers. Second, the layers deposited previously still contain some of the heat from previous passes, acting as a pre-heated base and increasing the initial temperature of each new layer. Third, the thin single-bead

wall has only a narrow cross-section through which heat can travel downward. The net result is an increase in average temperature in the upper wall and progressively higher melt-pool peaks for a given heat input until a quasi-steady balance between heat input and heat loss is approached; in the present build the H13 peaks change by less than 20 °C between layers 5 and 7 (2454, 2464 and 2472 °C), showing that this balance is effectively reached at the top of the H13 section.

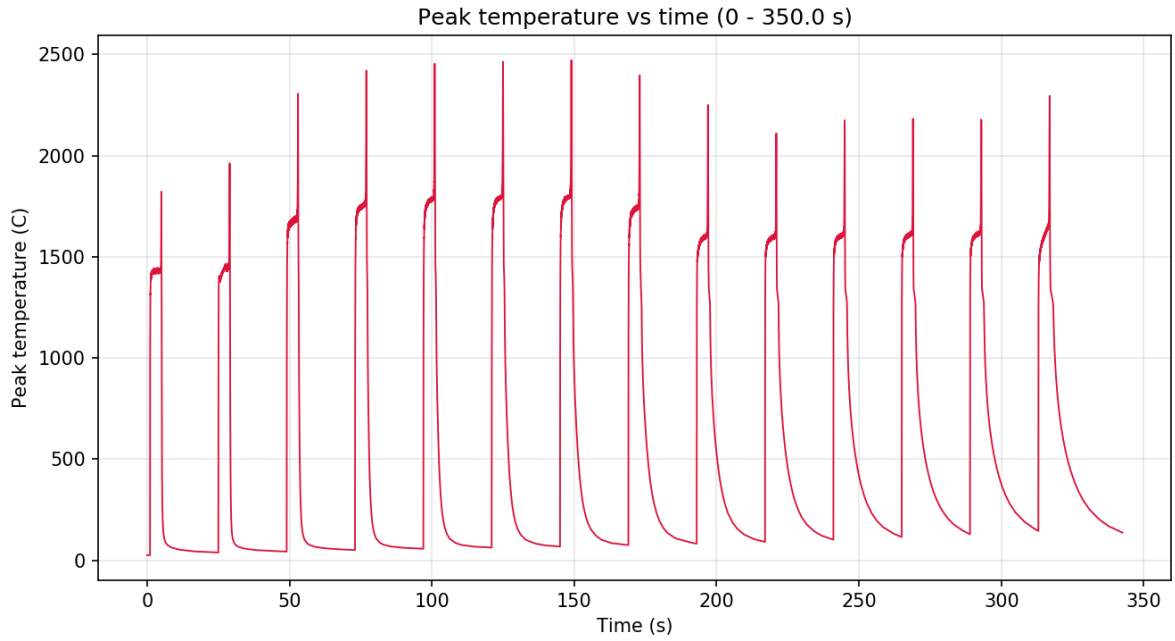

Figure 8.1. *Peak temperature as a function of time.*

At layer D8 the deposited material changes from H13 to IN718 (Figure 8.2). Because the same heat-source efficiency is used for both alloys (Section 7.2), the change in the thermal response at the interface is caused by the material properties alone. The first IN718 layer still reaches about 2397 °C — only some 75 °C below the last H13 layer — because it is deposited onto the strongly pre-heated H13 top. Over the next two layers the peak falls to about 2110 °C and then settles at a quasi-steady 2110–2180 °C for layers D10–D13, showing that the system reaches a new thermal equilibrium in the IN718 section. Two properties of IN718 drive this adjustment: its lower liquidus and solidus shift melting to lower temperatures, and its conductivity dataset rises to an effective 100 $mW \cdot mm^{-1} \cdot K^{-1}$ above ≈1344 °C to represent melt-pool convection (Section 3.4), which spreads the absorbed heat over a larger pool and lowers the peak. The result is a smooth, property-driven transition rather than a discontinuity in the energy input.

Finally, an increase of the peak temperature to about 2295 °C is observed at layer D14, even though the final layer uses a slightly reduced efficiency (Section 7.2). After several layers of

stable thermal behavior, the heat retained within the structure is large enough to overcome the heat-dissipation mechanisms; the last deposited layer — which has a permanently free top surface and is not followed by an interlayer dwell — therefore experiences a renewed thermal build-up and attains a higher peak temperature than the preceding layers.

In general, the thermal evolution shows that the cumulative heat accumulation and the properties of the two dissimilar materials have a strong effect on the temperature distribution during the multi-material deposition process. Due to the shared nodes between layers, the numerical model assumes a perfectly bonded interface, allowing heat to transfer across the H13/IN718 boundary without contact resistance, which is a slight idealization of the real interfacial heat transfer behavior.

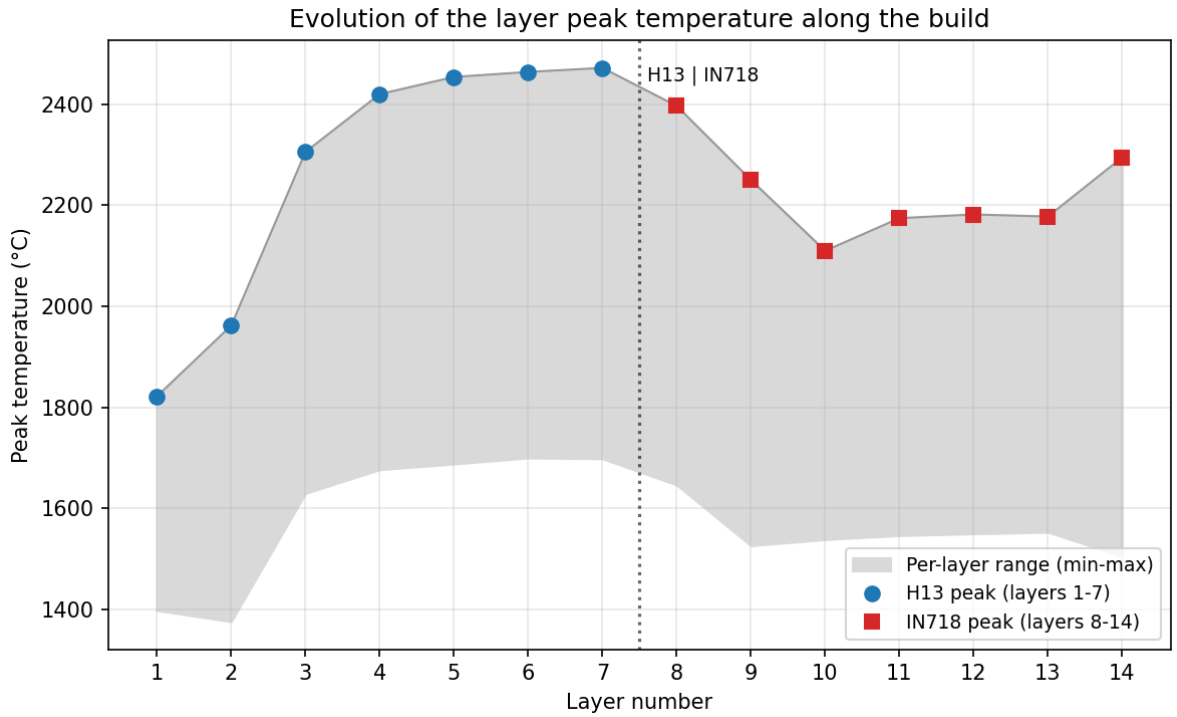

Figure 8.2. *Evolution of the layer peak temperature along the build, including the H13-to-IN718 transition.*

8.2 Printability analysis

This section evaluates the printability of the H13–IN718 build through the three indexes derived from the computed thermal field: the lack-of-fusion ratio, which measures the interlayer bonding; the non-dimensional thermal-strain parameter ε^*, which measures the susceptibility to distortion; and the composition change caused by the selective vaporization of volatile alloying elements.

8.2.1 Fusion and interlayer bonding

Fusion quality between the subsequently deposited layers plays an important role in the Directed Energy Deposition (DED) process, since it directly influences the structural integrity of the final component. The lack-of-fusion parameter (*LF*) can be used to evaluate the interlayer bonding and is defined as [33]:

$$LF = \frac{d}{h} \tag{8.1}$$

where d is the penetration depth of the melt pool and h is the height of the deposited layer. This parameter expresses the degree of remelting of the previously deposited layer and therefore the quality of the metallurgical bond between layers: when $LF \geq 1$ the melt pool is at least as deep as one layer and penetrates through the current layer to remelt the one beneath it (or the substrate, for the first layer), which is the condition for a sound bond, whereas when $LF < 1$ an un-melted band of thickness ($h - d$) remains at the interface and acts as a source of lack-of-fusion porosity. [14]

In this study the deposited layer height was kept constant at h = 0.8 mm, whereas the penetration depth varied during deposition according to the local thermal conditions described in Section 8.1.2. The predicted penetration depth d and melt-pool length w of each layer are shown in Figure 8.3; w denotes the extent of the pool along the scan direction (its length, not its width), and it is this length that enters the Fourier number of the thermal-strain analysis in Section 8.2.2, following the definition of [10].

The corresponding lack-of-fusion ratio is shown in Figure 8.4. The depth increases monotonically as the wall grows, from 0.60 mm in the first layer to 2.20 mm at the top of the H13 section and on to 3.00 mm in the uppermost layer — a direct consequence of the heat accumulation described in Section 8.1.2: the first layer solidifies against the cold substrate and forms only a shallow pool, whereas the hotter upper layers form progressively deeper pools. In contrast to the peak temperature, the depth shows no reduction at the material transition: the first IN718 layer melts slightly deeper (2.40 mm) than the last H13 layer, because the lower liquidus of IN718 (≈1337 °C against ≈1454 °C) lets the melt boundary reach farther for a comparable thermal field.

The melt-pool length follows the same qualitative trend. Within the H13 section it rises from 0.60 mm at the first layer to 2.60 mm at layer 7, driven by the surface peak temperature, which climbs with the heat accumulation described in Section 8.1.2.

Across the change of alloy the length increases markedly, from 2.60 mm to 3.60 mm at layer 8, then remains almost constant at 3.4–3.8 mm through the quasi-steady IN718 plateau, and

finally rises to its maximum of 4.80 mm at the last layer, where the renewed heat build-up — no longer followed by an interlayer dwell — again lengthens the pool. The longer pools of the IN718 section at similar or lower peak temperatures are, like the greater depth, a consequence of the lower liquidus of IN718 together with its high effective liquid conductivity (Section 3.4), which spreads the absorbed heat over a wider molten region. The molten region in the IN718 section is therefore both longer and deeper than in the H13 section, although its peak temperature is lower.

The lack-of-fusion ratio in Figure 8.4 shows the depth normalized by the layer height. The dashed line at $LF = 1$ marks the limiting condition $d = h$. Only the first layer falls below this threshold, with $LF = 0.75$: its 0.60 mm pool does not reach the substrate surface (which would require $d \geq 0.80$ mm), so a thin un-melted band of about 0.2 mm is left at the layer-1/substrate interface, indicating a risk of lack-of-fusion at the very bottom of the wall. From the second layer onward *LF* is everywhere at least 1.5 and rises up the build to a maximum of 3.75 at layer 14, so sound interlayer bonding is predicted throughout the remainder of the deposit.

The high *LF* values in the upper layers mean that each pass there remelts up to three or four previous layer heights. This degree of remelting follows directly from the geometry of the calibrated heat source and of the wall: the volumetric source penetrates $b = 1.6$ mm — two layer thicknesses — by construction (Section 7.2), and the thin 0.6 mm single-bead wall forces the absorbed heat to flow almost exclusively downward, so that on a pre-heated base the liquidus isotherm reaches well below the source itself. While this deep remelting ensures good fusion, it also implies substantial remelting and dilution of the already-deposited material, which is relevant to the local microstructure and composition.

Because the model joins the successive layers through shared nodes, as noted in Section 8.1.2, the interface is treated as perfectly bonded; the melt-pool depth and the *LF* ratio derived from it are therefore the physically meaningful indicators of where lack-of-fusion porosity would be expected — here only at the first layer and the substrate interface — rather than a direct measurement of porosity, which would require experimental examination of the wall.

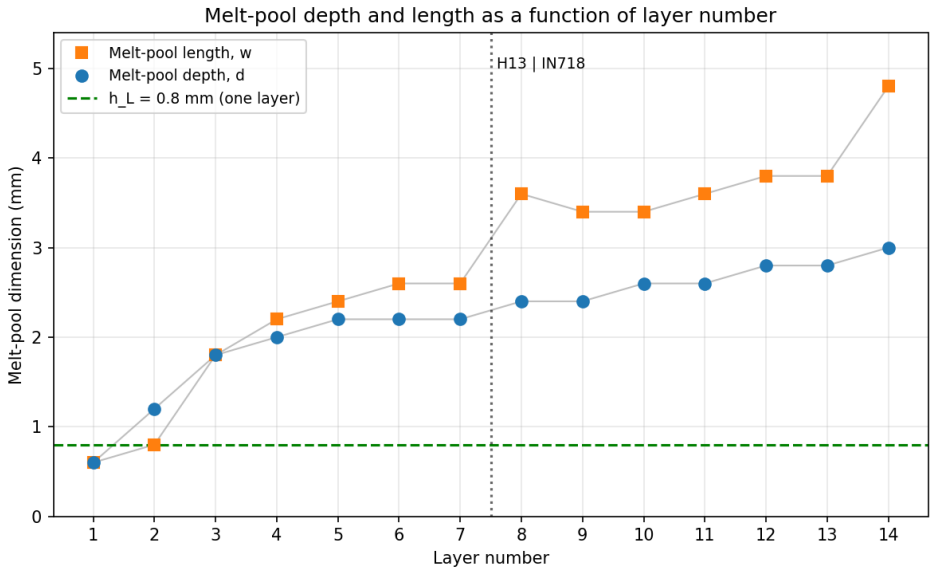

Figure 8.3. *Melt-pool depth and length as a function of layer number.*

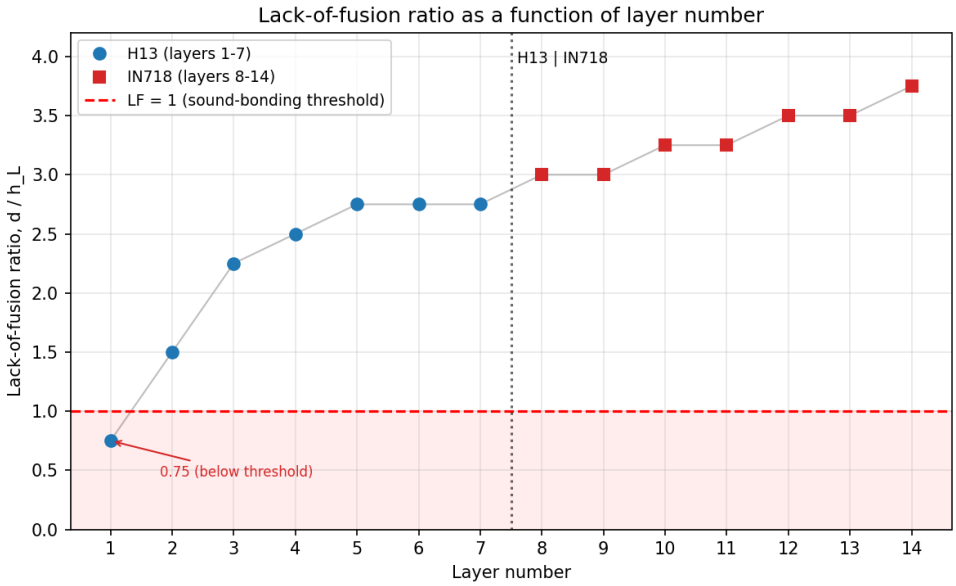

Figure 8.4. *Lack-of-fusion ratio as a function of layer number.*

8.2.2 Maximum thermal strain (Buckingham π theorem)

The tendency of the deposited structure to distort during the process can be assessed through the maximum thermal strain. A non-dimensional thermal-strain parameter ε^*, representative of the maximum thermal strain, can be predicted from a relation derived with the Buckingham π theorem [10]:

$$\varepsilon^* = \frac{\beta \Delta T}{EI} \frac{t}{F\sqrt{\rho}} H^{\frac{3}{2}} \tag{8.2}$$

In this relation, β is the volumetric coefficient of thermal expansion, which describes the tendency of a material to expand when heated. For isotropic materials it is related to the linear

thermal-expansion coefficient by $\beta = 3\alpha$, where α is the conventional linear coefficient of thermal expansion. The remaining quantities are:

- ΔT = difference between the peak temperature and the ambient temperature;
- t = deposition (scan) time of a layer;
- H = heat input per unit length, $H = \eta P/v$, where η is the absorptivity, P the laser power and v the scan speed;
- EI = flexural rigidity of the deposited structure, where E is the Young's modulus and I the second moment of area;
- F = Fourier number, $F = \alpha_d / (v \cdot w)$, where α_d is the thermal diffusivity, v the scan speed and w the melt-pool length;
- ρ = material density.

The parameter ε^* provides an estimate of the relative susceptibility of each layer to thermal strain. A higher temperature rise ΔT or a larger thermal-expansion coefficient increases ε^*, whereas a higher flexural rigidity EI reduces it. A larger melt pool also increases ε^*, because a longer pool lowers the Fourier number F, to which ε^* is inversely proportional. The parameter is therefore useful for assessing the thermo-mechanical behavior of the deposited multi-material structure. Figure 8.5 shows ε^* evaluated for each deposited layer, using the per-layer peak temperatures and melt-pool lengths obtained from the simulation together with the material properties of each alloy; the fixed inputs are collected in Table 8.2 and the per-layer values in Table 8.3.

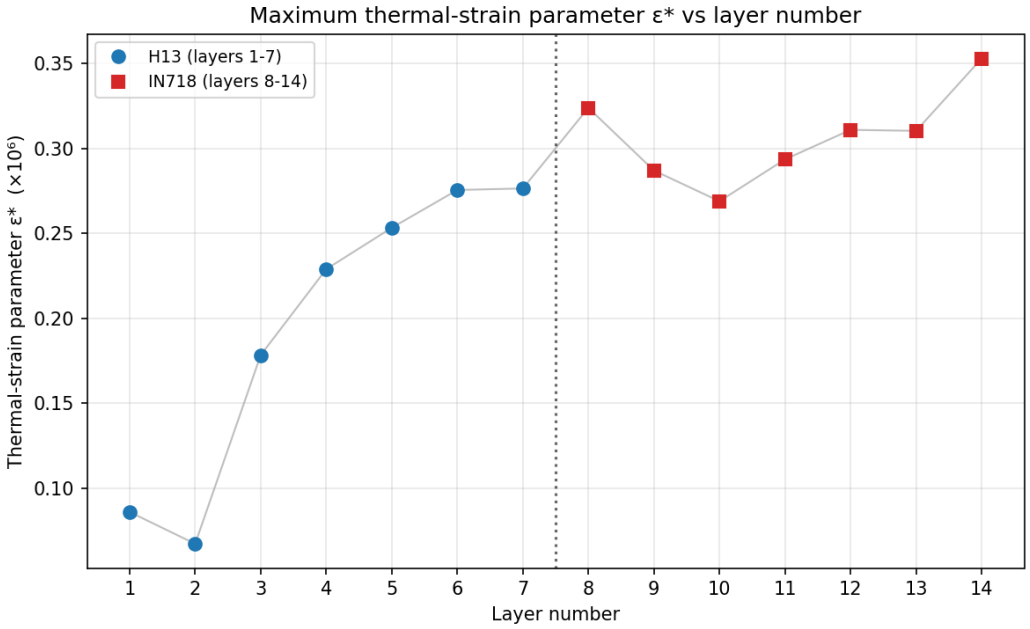

Figure 8.5. *Maximum thermal-strain parameter ε^* for each deposited layer.*

Within the H13 section (layers 1–7) the thermal-strain parameter first dips slightly, from 0.086×10^6 at the first layer to 0.067×10^6 at layer 2 — the first layer carries a higher heat input per unit length because of its first-layer efficiency (Section 7.2) — and then rises with the heat accumulation to 0.28×10^6 at layer 7, roughly a three-fold increase across the section. Two quantities grow together as the wall builds up: the temperature rise ΔT, since the heat accumulation described in Section 8.1.2 raises the peak temperature of each successive layer, and the melt-pool length w, which increases from 0.6 mm to 2.6 mm. A longer pool lowers the Fourier number $F = \alpha_d / (v \cdot w)$, and because ε^* is inversely proportional to F, the two effects reinforce one another.

At the transition from H13 to IN718 (layer 8) the parameter rises further, to about 0.32×10^6: the IN718 pools are longer (3.6 mm against 2.6 mm), and the resulting drop of the Fourier number outweighs the smaller thermal-expansion coefficient of IN718 (β = 30×10^{-6} against 43.5×10^{-6} K^{-1}). Through layers 9–13 the parameter remains almost constant at ≈ 0.27–0.31×10^6, mirroring the quasi-steady thermal plateau, and it reaches its maximum of 0.35×10^6 at the final layer, which combines the highest IN718 peak temperature of the plateau region with the longest melt pool of the build.

The maximum susceptibility to thermal strain therefore occurs at the last deposited layer, and — once a single, material-independent efficiency is used — the profile across the two alloys is comparatively uniform: the property differences between H13 and IN718 (a larger expansion coefficient for H13; longer pools and a lower Young's modulus for IN718) largely offset one another, so ε^* is governed primarily by the heat accumulation along the build rather than by the change of material.

It should be emphasized that ε^* is a dimensionless parameter representative of the maximum thermal strain, not the thermal strain itself. Its absolute magnitude depends on the chosen reference quantities — in particular the flexural rigidity EI and the melt-pool length used in the Fourier number — so it should be read as a relative measure of each layer's susceptibility to thermal distortion rather than as an absolute strain.

Because the present model is a heat-transfer analysis, the actual strain and residual-stress fields are not computed; obtaining them would require a sequentially coupled thermo-mechanical analysis, using this temperature history together with the temperature-dependent mechanical properties (E, ν, yield strength) of the two alloys. [21]

Table 8.2. *Fixed inputs and material properties*

Symbol	Quantity	H13 (layers 1–7)	IN718 (layers 8–14)	Units	How obtained
P	Laser power	250	250	W	process input
v	Scan speed	5×10^{-3}	5×10^{-3}	m/s	process input (5 mm/s)
t	Deposition time	4	4	s	scan length ÷ speed (20 mm ÷ 5 mm/s)
L	Wall length	0.020	0.020	m	geometry
b	Wall thickness	6×10^{-4}	6×10^{-4}	m	geometry (0.6 mm)
I	Second moment of area	3.6×10^{-13}	3.6×10^{-13}	m⁴	$I = L\cdot b^3 / 12$
T_0	Ambient temperature	25	25	°C	model setting
α	Linear thermal expansion	14.5×10^{-6}	10.0×10^{-6}	1/K	material data [11], [13]
β	Volume expansion	43.5×10^{-6}	30×10^{-6}	1/K	$\beta = 3\alpha$
ρ	Density	7760	8220	kg/m³	material data [24], [13]
E	Young's modulus	207×10^{9}	165×10^{9}	Pa	material data [24], [13]
k	Thermal conductivity	28.6	26.6	W/(m·K)	material data [11], [9]
c_p	Specific heat	658	600	J/(kg·K)	material data [11], [9]
α_d	Thermal diffusivity	5.60×10^{-6}	5.39×10^{-6}	m²/s	$= k / (\rho\cdot c_p)$
η	Absorptivity	0.30 for layers 2–7; 0.45 for layer 1	0.30 for layers 8–13; 0.27 for layer 14	–	heat-source efficiency
H	Heat input per unit length	15000 for layers 2–7; 22500 for layer 1	15000 for layers 8–13; 13500 for layer 14	J/m	$H = \eta\cdot P / v$
EI	Flexural rigidity	0.0745	0.0594	N·m²	$EI = E\cdot I$

Table 8.3. *Per-layer values used in the ε* plot*

Layer	Material	Peak T, °C	ΔT (K)	w (mm)	F	ε^*
1	H13	1822	1797	0.60	1.867	8.61×10^{4}

Layer	Material	Peak T, °C	ΔT (K)	w (mm)	F	ε^*
2	H13	1962	1937	0.80	1.400	6.74×10^{4}
3	H13	2306	2281	1.80	0.622	1.78×10^{5}
4	H13	2420	2395	2.20	0.509	2.29×10^{5}
5	H13	2454	2429	2.40	0.467	2.53×10^{5}
6	H13	2464	2439	2.60	0.431	2.76×10^{5}
7	H13	2472	2447	2.60	0.431	2.77×10^{5}
8	IN718	2397	2372	3.60	0.300	3.24×10^{5}
9	IN718	2250	2225	3.40	0.317	2.87×10^{5}
10	IN718	2110	2085	3.40	0.317	2.69×10^{5}
11	IN718	2175	2150	3.60	0.300	2.94×10^{5}
12	IN718	2182	2157	3.80	0.284	3.11×10^{5}
13	IN718	2178	2153	3.80	0.284	3.10×10^{5}
14	IN718	2295	2270	4.80	0.225	3.53×10^{5}

8.2.3 Vaporization of alloying elements and composition change

During the Directed Energy Deposition process, the extremely high temperature generated inside the melt pool may cause partial vaporization of the volatile alloying elements, and the effect becomes more pronounced as the local temperature increases [12]. This leads to gradual changes in the chemical composition of the deposited material, and such elemental loss may affect the final mechanical and metallurgical properties of the manufactured structure.

The vaporization flux of an alloying element can be estimated from the Langmuir evaporation relation [33]:

$$J_i = \frac{\lambda P_i}{\sqrt{2\pi M_i T R}} \tag{8.3}$$

Where J_i is the evaporation flux, P_i is the vapor pressure of element i over the alloy, M_i is its molecular mass, R is the universal gas constant, T is the local (melt-pool) temperature, and λ (= 0.05) is a correction factor associated with the condensation of vaporized atoms [33]. The relation shows that evaporation increases markedly with the melt-pool temperature. In the present work the flux is evaluated in its mass form (the molar flux multiplied by the molar mass), so that the evaporated quantity is obtained directly as a mass.

The vapor pressure of an element over the alloy is taken as [34]:

$$P_i = X_i . P_i^{\circ}(T) \tag{8.4}$$

Where X_i is the mole fraction of the element i in the alloy and $P_i^{\circ}(T)$ is the equilibrium vapor pressure of the pure element i at temperature T. The pure-element vapor pressures are taken

from the CRC Handbook vapor-pressure table [22], which lists the temperature at which each element reaches a given pressure. Over the melt-pool temperature range these data follow a relation of the form, namely:

$$log_{10}\left(\frac{P}{P_a}\right) = 11.19 - \frac{18194}{T} \qquad \text{(Cr)} \tag{8.5}$$

$$log_{10}\left(\frac{P}{P_a}\right) = 10.27 - \frac{12290}{T} \qquad \text{(Mn)} \tag{8.6}$$

The element considered in each section is the one with the highest vapor pressure: manganese in the H13 layers and chromium in the IN718 layers.

The total mass of an element evaporated during the deposition of a layer is approximated by [34]:

$$\Delta m_i = \frac{L \times A_S \times J_i}{v} \tag{8.7}$$

where L is the deposition length, A_s is the melt-pool surface area, v is the scan speed and J_i is the evaporation flux. The melt-pool surface area is taken $A_s = w \cdot b$, the melt-pool length w (obtained from the simulation) times the wall thickness b. The corresponding change in composition follows from a mass balance [34]:

$$W_f = \frac{V\rho W_i - \Delta m_i}{V\rho - \sum \Delta m_i} \tag{8.8}$$

where V is the volume of the deposited layer, ρ its density, W_i is the initial weight fraction of the element and $\sum \Delta m_i$ is the total evaporated mass. In this way the only quantities taken from the simulation are the melt-pool temperature and the melt-pool size; the molar masses, boiling points, heats of vaporization and alloy compositions are material data.

Table 8.4. *Nominal compositions of H13 and IN718, in wt%* [15], [17]

Element	H13, wt%	IN718, wt%
Fe	Balance (≈ 90.6)	≈ 18.5
Ni	—	52.5
Cr	5.00	18.5
Nb	—	5.1
Mo	1.50	3.0
Ti	—	0.9
Al	—	0.5
V	1.00	—
Mn	0.35	0.20
Si	1.00	0.20
C	0.40	0.04

Calculation procedure:

1. Choosing the volatile element of each section (Mn in H13, Cr in IN718).
2. Taking the melt-pool temperature T of each layer from the simulation, and the melt-pool surface area A_s = w × wall thickness (0.6 mm), using the melt-pool length w from the simulation. Because the Langmuir relation is valid only up to the boiling point of the element, T is taken as the highest surface temperature of the layer (the whole-model peak) wherever that value lies below the element's boiling point — all IN718 layers for chromium, and layers 1–2 for manganese — and as the representative mid-track melt-pool temperature (the peak of the fixed mid-length node used in Section 8.3.2) for the H13 layers 3–7, whose surface maximum exceeds the manganese boiling point. The instantaneous surface maximum of those layers is a brief, localized numerical spike under the beam (Section 9); evaluating the whole-pool, whole-scan mass balance of Eq. (8.7) at that value would overestimate the loss by construction, and the corresponding figures are therefore quoted only as upper bounds.
3. Reading the pure-element vapor pressure $P_i°(T)$from the CRC Handbook vapor-pressure table, fitted over the melt-pool range as $log_{10}\left(\frac{P}{P_a}\right) = a - \frac{b}{T}$
4. Getting the vapor pressure over the alloy, $P_i = X_i . P_i°(T)$, here x_i is the mole fraction of the element in the alloy.
5. Computing the mass evaporation flux J, then the mass evaporated Δm during one scan (Eq. 8.7), then the new composition W_f (Eq. 8.8).

Input data (Tables 8.4–8.6):

Tracked elements:

Table 8.5. *Properties of the tracked volatile elements (Mn in H13, Cr in IN718).* [22]

Element	M, g/mol	Boiling point, °C	mole fraction x_i	initial W_i, wt%
Mn (in H13)	54.94	2061	0.00348	0.35
Cr (in IN718)	52.00	2671	0.207	18.5

Constants, process and geometry:

Table 8.6. *Constants, process parameters and geometry used in the vaporization estimate.*

Quantity	Value	Note
λ (condensation factor)	0.05	[33]

Quantity	Value	Note
R (gas constant)	8.314 J/(mol·K)	—
L (deposition length)	0.020 m	geometry
v (scan speed)	5×10^{-3} m/s	process
A_s (melt-pool area)	w × 0.6 mm	w from simulation per layer
V (layer volume)	9.6×10^{-9} m³	L × 0.6 mm × 0.8 mm
ρ (H13 / IN718)	7760 / 8220 kg/m³	material data

The predicted vaporization and composition change per layer are given in Tables 8.7 and 8.8.

H13 section (Mn):

Table 8.7. *Predicted vaporization and composition change in the H13 section (manganese).*

Layer	T_{used}, °C	P_i, P_a	J, kg m^{-2} s^{-1}	Δm_i (mg)	Loss (%)	W_f, wt%	Upper bound (%)
1	1822 (surface max)	88.2	0.0031	0.005	1.7	0.34	—
2	1962 (surface max)	206	0.0071	0.014	5.2	0.33	—
3	1686 *	34.6	0.0013	0.006	2.1	0.34	58.8
4	1755 *	56.4	0.0020	0.011	4.1	0.34	112
5	1785 *	69.0	0.0025	0.014	5.5	0.33	139
6	1792 *	72.5	0.0026	0.016	6.2	0.33	156
7	1795 *	74.1	0.0026	0.017	6.3	0.33	160

** Representative mid-track pool temperature; the surface maximum of these layers (2306–2472 °C) exceeds the Mn boiling point (2061 °C), so the value obtained at the surface maximum — last column — is only an upper bound (step 2).*

IN718 section (Cr):

Table 8.8. *Predicted vaporization and composition change in the IN718 section (chromium).*

Layer	T, °C	P_i, P_a	J, kg m^{-2} s^{-1}	Δm_i (mg)	Loss (%)	W_f, wt%
8	2397	4913	0.150	1.30	8.9	17.14
9	2250	1976	0.062	0.51	3.5	17.97
10	2110	744	0.024	0.20	1.3	18.30
11	2175	1183	0.038	0.33	2.2	18.16
12	2182	1246	0.040	0.36	2.5	18.12
13	2178	1210	0.039	0.35	2.4	18.14
14	2295	2638	0.082	0.95	6.5	17.51

In the IN718 section the melt-pool temperatures remain well below the boiling point of chromium (2671 °C), so the Langmuir relation is applied directly at the surface maximum of each layer and the estimates can be treated quantitatively. The chromium loss follows the peak-

temperature profile of Section 8.1.2: it is largest at the two hottest layers — about 8.9 % at layer 8, where the pool sits on the pre-heated H13 top, and about 6.5 % at the final layer — and stays between 1.3 % and 2.5 % along the quasi-steady plateau. Even in the worst layer the chromium content falls only from 18.5 wt% to about 17.1 wt%.

In the H13 section the first two layers also remain below the boiling point of manganese (2061 °C) and give small losses (1.7 % and 5.2 %). For layers 3–7 the surface maximum exceeds the manganese boiling point, so the loss is evaluated at the representative mid-track pool temperature (1686–1795 °C); it rises with the heat accumulation from 2.1 % to 6.3 %, corresponding to a manganese content that never falls below about 0.33 wt%. The last column of Table 8.7 lists the value obtained if the same mass balance is instead evaluated at the instantaneous surface maximum: because the Langmuir relation diverges above the boiling point and Eq. (8.7) applies that flux over the entire pool for the entire scan, these figures are quoted only as upper bounds without physical meaning — reaching or exceeding 100 % for the hotter layers (4–7) and staying below it only at layer 3.

The following points define the reliability of these estimates:

- The Langmuir relation assumes free evaporation and overestimates the loss once the vapor pressure approaches the surrounding pressure; this is why the upper-bound column of Table 8.7 is not used quantitatively.
- At the surface maxima of layers 3–7 the vapor pressures would be extrapolated beyond the range of the CRC table, which ends at 1 atm (reached at the boiling point); the representative pool temperatures remain inside the tabulated range.
- The instantaneous surface maximum contains the brief, localized spike discussed in Section 9, to which the exponential vapor-pressure dependence is extremely sensitive; the representative mid-track temperature is free of it.
- An ideal solution is assumed ($P_i = X_i . P_i°(T)$).

In summary, selective vaporization remains limited across the build. The predicted losses of both elements are of the order of a few percent — in absolute terms at most ≈ 0.02 wt% of manganese and ≈ 1.4 wt% of chromium — increasing with the local peak temperature set by the heat accumulation and largest at the hottest layers of each section. These magnitudes are consistent with the small vaporization-induced composition changes reported for laser additive manufacturing in previous studies [14], [33].

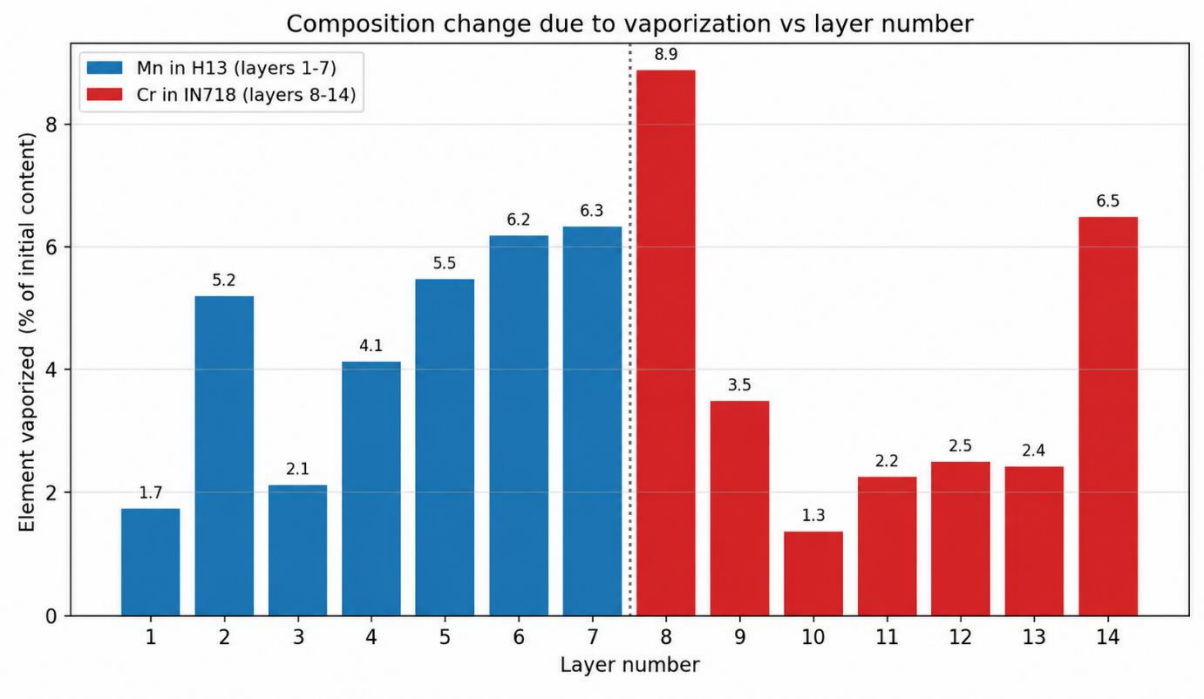

Figure 8.6. *Predicted composition change caused by selective vaporization along the build; the H13 values of layers 3–7 are evaluated at the representative mid-track pool temperature (Table 8.7).*

8.3 Cooling behavior and solidification structure

8.3.1 Cooling behavior

After deposition of the last layer, the simulation entered a cooling stage, where the heat source was shut off and the structure dissipated heat through its external surfaces. The maximum temperature in the wall was approximately 2295 °C at the end of deposition. In the first moments of cooling the maximum temperature fell extremely rapidly: it dropped below the IN718 liquidus (≈1337 °C) within about 0.4 s and reached about 761 °C within three seconds, indicating a very strong initial heat dissipation driven by the large temperature difference to the surroundings and by the release of the heat stored in the melt pool. By continued cooling, the temperature gradually decreased in the whole deposited wall and substrate.

The upper part of the wall remained much hotter than the lower for a longer time, indicating that heat accumulated during deposition took longer to dissipate through the structure. The substrate served as the main heat sink and removed heat from the deposited material by conduction.

Because the temperature difference between the part and the environment was large, the cooling rate was highest right after deposition. As the temperature decreased the heat loss became slower and the thermal gradients decreased across the structure. At the end of the

cooling step, at around 2117 s of total simulation time, the whole model was near the ambient temperature with values near 27–30 °C (Table 8.9).

Table 8.9. *Temperature field at successive stages of the cooling step.*

Stages	Thermal Contour
1	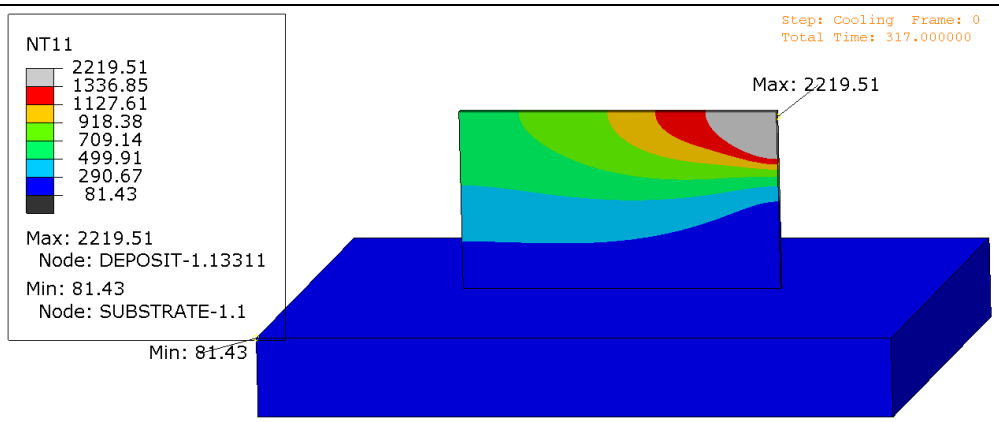
2	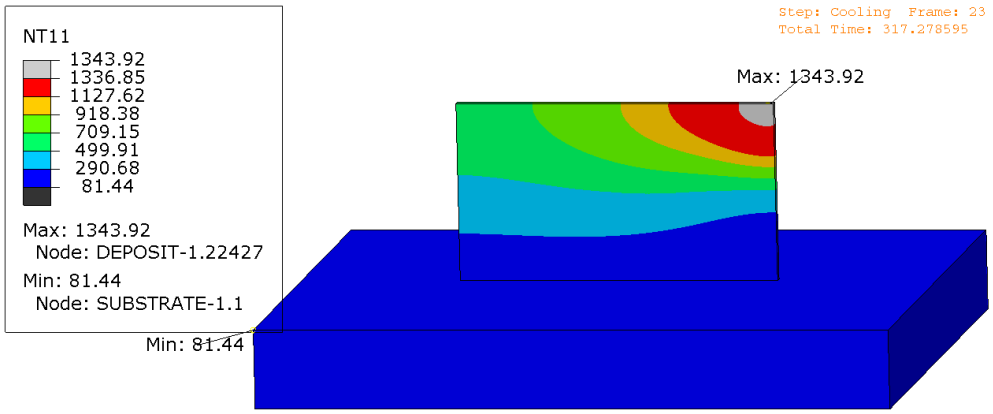
3	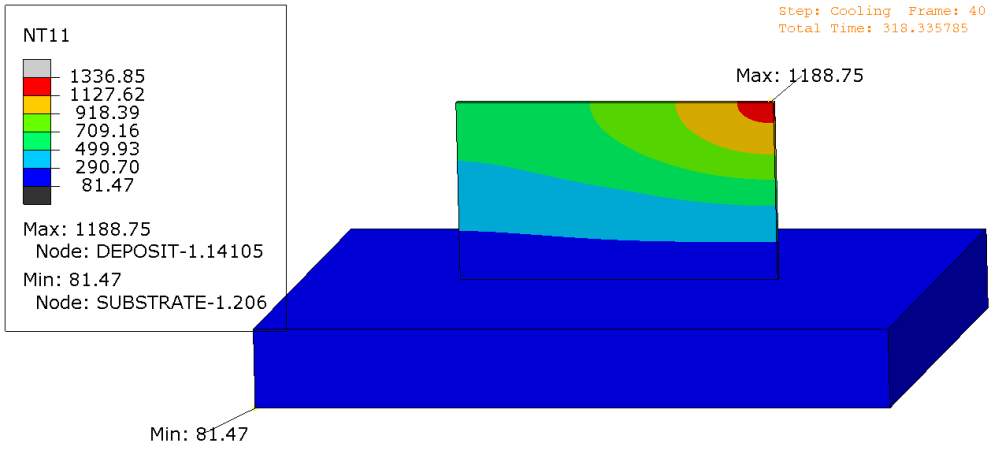

4	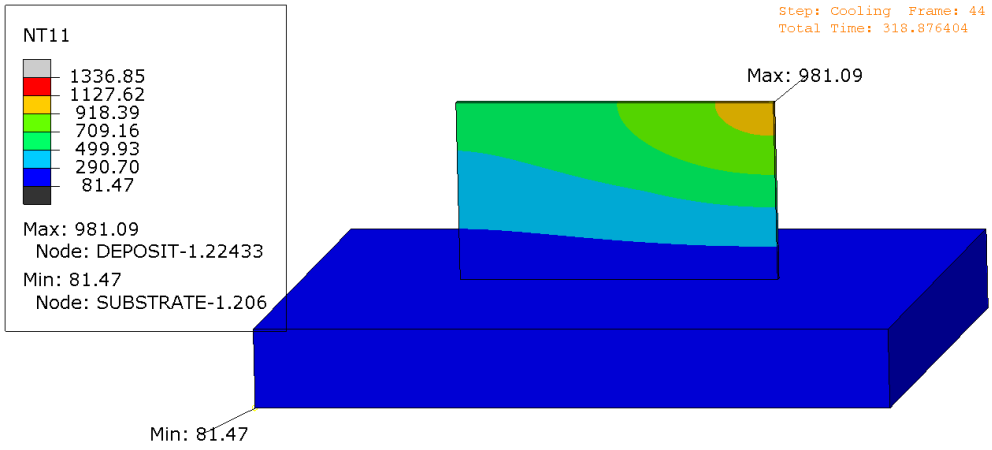 NT11 1336.85 1127.62 918.39 709.16 499.93 290.70 81.47 Max: 981.09 Node: DEPOSIT-1.22433 Min: 81.47 Node: SUBSTRATE-1.206 Step: Cooling Frame: 44 Total Time: 318.876404 Max: 981.09 Min: 81.47
5	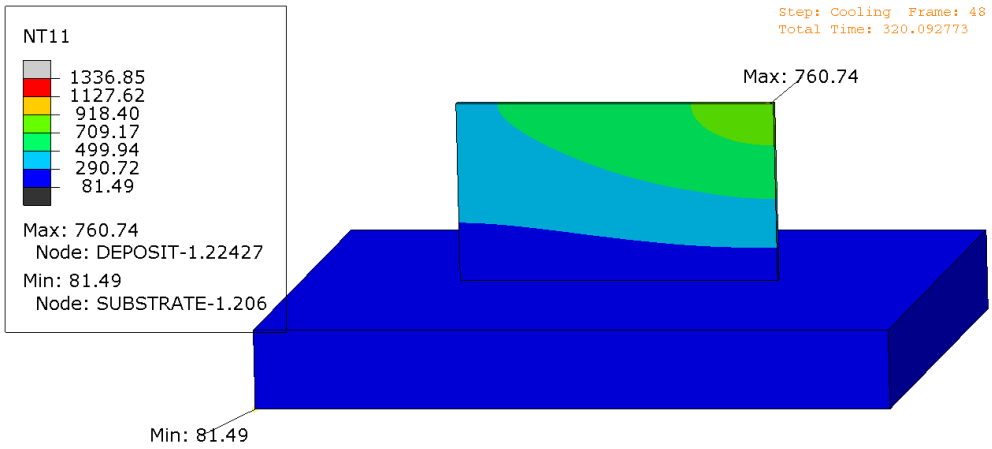 NT11 1336.85 1127.62 918.40 709.17 499.94 290.72 81.49 Max: 760.74 Node: DEPOSIT-1.22427 Min: 81.49 Node: SUBSTRATE-1.206 Step: Cooling Frame: 48 Total Time: 320.092773 Max: 760.74 Min: 81.49
6	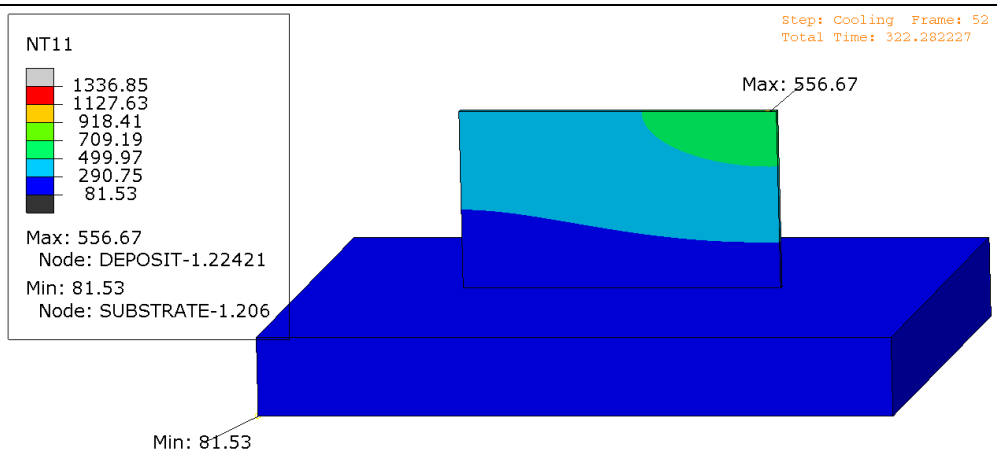 NT11 1336.85 1127.63 918.41 709.19 499.97 290.75 81.53 Max: 556.67 Node: DEPOSIT-1.22421 Min: 81.53 Node: SUBSTRATE-1.206 Step: Cooling Frame: 52 Total Time: 322.282227 Max: 556.67 Min: 81.53
7	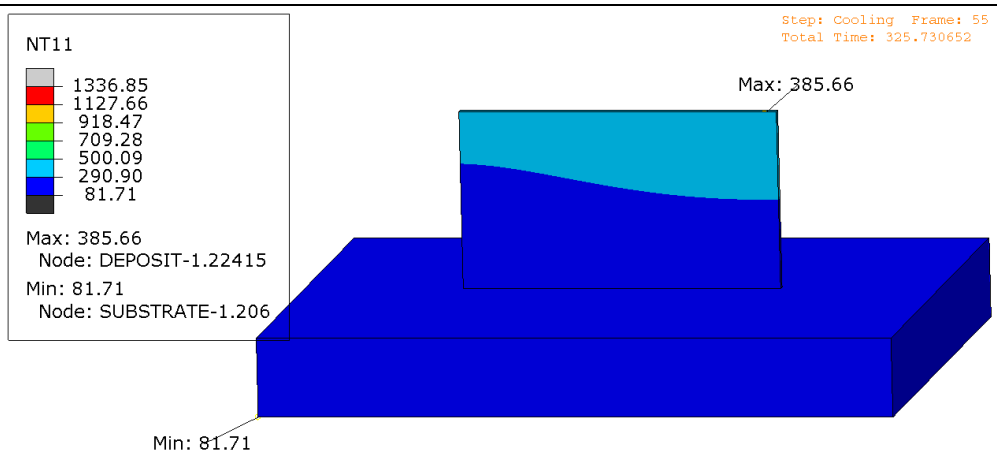 NT11 1336.85 1127.66 918.47 709.28 500.09 290.90 81.71 Max: 385.66 Node: DEPOSIT-1.22415 Min: 81.71 Node: SUBSTRATE-1.206 Step: Cooling Frame: 55 Total Time: 325.730652 Max: 385.66 Min: 81.71

8	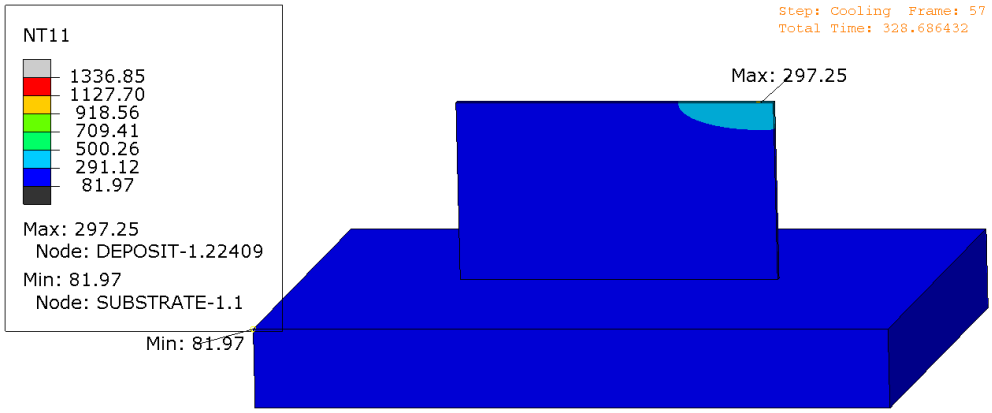 NT11 1336.85 1127.70 918.56 709.41 500.26 291.12 81.97 Max: 297.25 Node: DEPOSIT-1.22409 Min: 81.97 Node: SUBSTRATE-1.1 Step: Cooling Frame: 57 Total Time: 328.686432 Max: 297.25 Min: 81.97
9	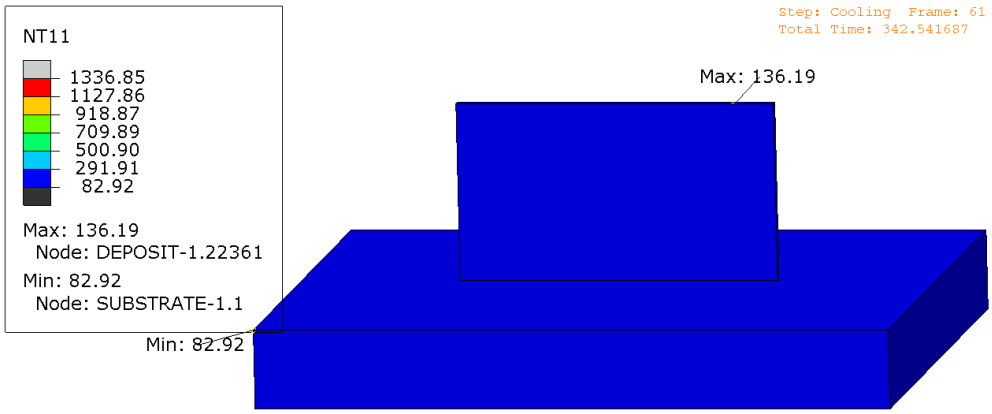 NT11 1336.85 1127.86 918.87 709.89 500.90 291.91 82.92 Max: 136.19 Node: DEPOSIT-1.22361 Min: 82.92 Node: SUBSTRATE-1.1 Step: Cooling Frame: 61 Total Time: 342.541687 Max: 136.19 Min: 82.92
10	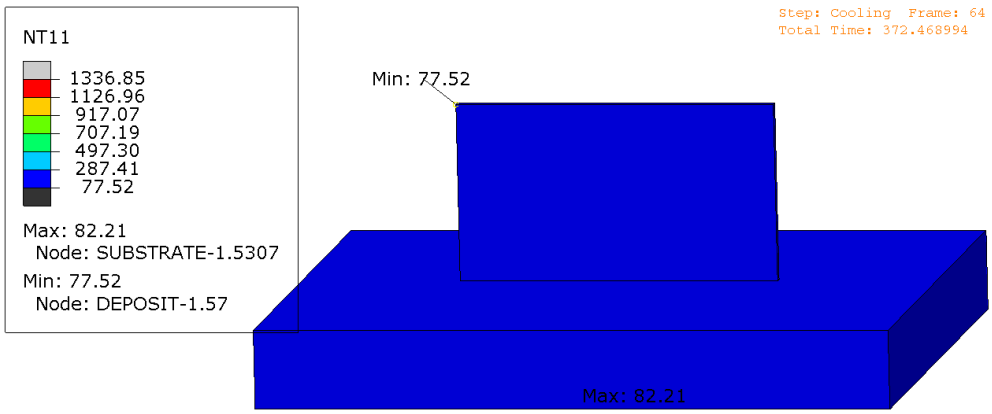 NT11 1336.85 1126.96 917.07 707.19 497.30 287.41 77.52 Max: 82.21 Node: SUBSTRATE-1.5307 Min: 77.52 Node: DEPOSIT-1.57 Step: Cooling Frame: 64 Total Time: 372.468994 Min: 77.52 Max: 82.21
11	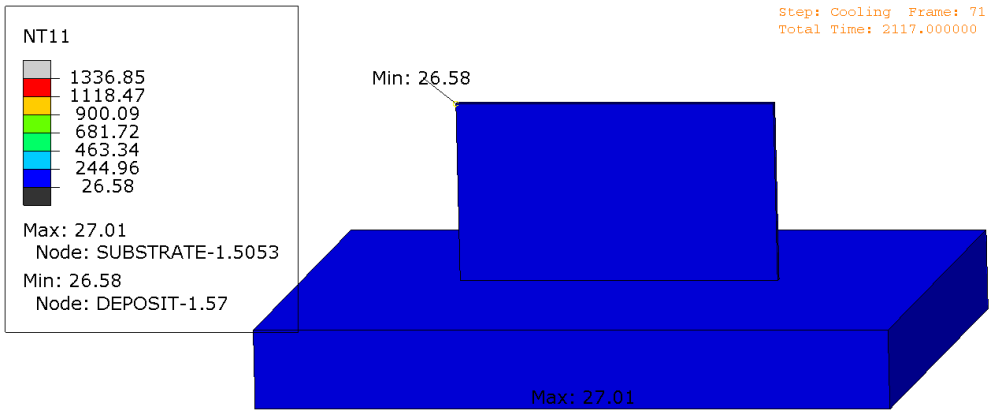 NT11 1336.85 1118.47 900.09 681.72 463.34 244.96 26.58 Max: 27.01 Node: SUBSTRATE-1.5053 Min: 26.58 Node: DEPOSIT-1.57 Step: Cooling Frame: 71 Total Time: 2117.000000 Min: 26.58 Max: 27.01

8.3.2 Cooling Rate and Secondary Dendrite Arm Spacing

The cooling rate is the rate at which the deposited material cools down after melting. This has a direct influence on the structure of solidification formed during deposition. This parameter controls the scale of the microstructure produced in the solidified material. The relationship between the cooling rate and the resulting microstructural refinement can be expressed as [35]:

$$\lambda = b(CR)^{-n} \tag{8.9}$$

where λ is the secondary dendrite arm spacing, CR is the cooling rate, and b and n are constants that depend on the alloy. The equation shows that the secondary dendrite arm spacing decreases as the cooling rate increases: faster cooling gives smaller λ and a finer dendritic structure, while slower cooling gives larger λ and a coarser microstructure [23]. The cooling rate of each layer was obtained from its thermal cycle as the average rate of temperature drop across the solidification (mushy-zone) interval, that is:

$$CR = \frac{T_{liquidus} - T_{solidus}}{t_{solidus} - t_{liquidus}} \tag{8.10}$$

evaluated at the center of each layer during its primary solidification, where $t_{liquidus}$ and $t_{solidus}$ are the times at which the material passes through the liquidus and solidus temperatures. The secondary dendrite arm spacing was then calculated from, using the material constants b = 80 and n = 0.33 for the H13 (steel) section and b = 39.8 and n = 0.3 for the IN718 (nickel-based superalloy) section. [35] The results are listed in Table 8.10 and plotted in Figure 8.7. Layers 1 and 2 are not listed: their central nodes did not reach the liquidus temperature in the analysis (a cold-substrate boundary effect at the bottom of the wall, consistent with the shallow pools of Section 8.2.1), so no solidification cooling rate could be extracted for them.

Table 8.10. *Cooling rate and secondary dendrite arm spacing of each deposited layer.*

Layer	Material	Cooling rate *CR*, °C/s	SDAS λ, µm
3	H13	1695	6.88
4	H13	1258	7.59
5	H13	1030	8.11
6	H13	928	8.39
7	H13	884	8.53
8	IN718	494	6.19
9	IN718	336	6.95
10	IN718	285	7.30
11	IN718	251	7.59
12	IN718	229	7.80

Layer	Material	Cooling rate *CR*, °C/s	SDAS λ, µm
13	IN718	215	7.94
14	IN718	154	8.78

The cooling rate is highest in the first listed layers and decreases steadily up the build in both sections — from about 1695 °C/s near the bottom of the H13 section (layer 3) to about 884 °C/s at its top, and from about 494 °C/s to 154 °C/s through the IN718 section. This reduction is caused by the heat accumulation described in Section 8.1.2: as the structure grows, each new layer cools progressively more slowly. At the start of the IN718 section (layer 8) the cooling rate falls markedly with respect to the last H13 layer (about 494 against 884 °C/s): the narrower solidification interval of IN718 (≈ 82 K against ≈ 139 K for H13) is crossed more slowly because of the latent-heat release and the strong effective liquid conductivity of the alloy, so the downward trend steepens at the change of alloy before flattening along the IN718 plateau. As a direct consequence, the secondary dendrite arm spacing increases up the build in both sections, from about 6.9 µm to 8.5 µm in the H13 and from about 6.2 µm to 8.8 µm in the IN718 section, indicating a progressive coarsening of the solidification structure toward the top of the part. The finer spacing at the beginning of the IN718 section follows from its different solidification constants (*b, n*) [35]. Because the thermal conditions change continuously during the multi-material build — through heat accumulation and the H13-to-IN718 transition — different regions solidify under different cooling conditions, producing the local variations in microstructural scale captured by λ. [24]

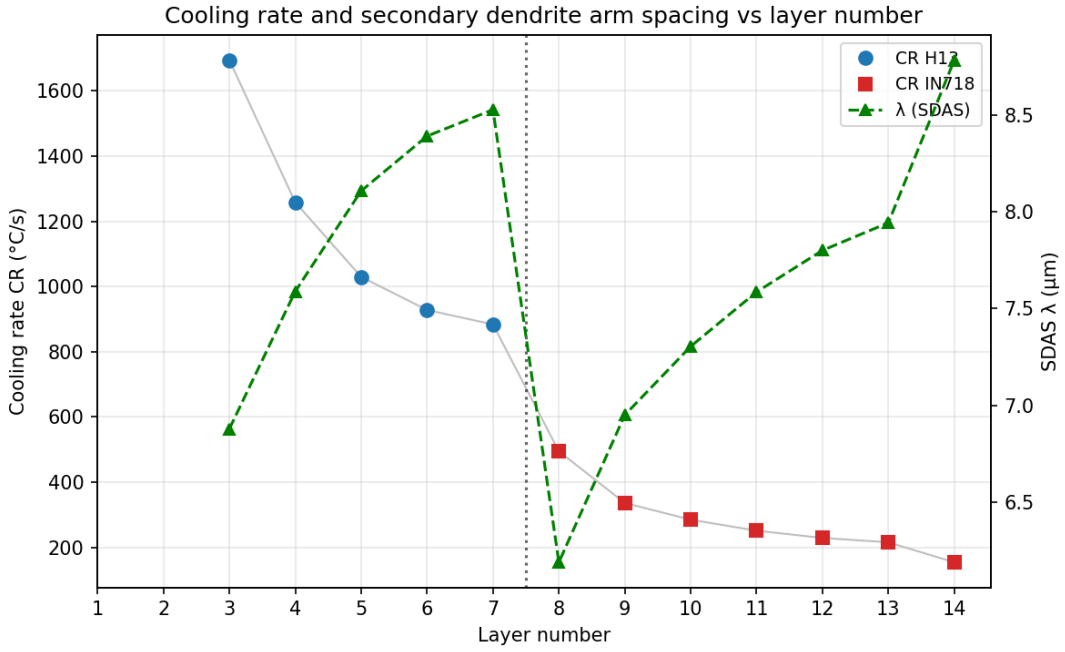

Figure 8.7. *Cooling rate and secondary dendrite arm spacing for each deposited layer.*

8.3.3 Solidification rate and morphology

The cooling conditions in the melt pool during solidification can be described by the combination of the temperature gradient G ahead of the solidification front and the solidification rate R. These two quantities are linked to the cooling rate through:

$$CR = G.R \tag{8.11}$$

where CR is the cooling rate, G is the thermal gradient ahead of the solidification front and R is the velocity of that front. Together, G and R control the way the liquid transforms to solid during deposition. [23]

The morphology of the solidification front depends strongly on the ratio G/R. The stability of a planar front is governed by the constitutional-supercooling criterion [36]:

$$\frac{G}{R} \geq \frac{m_L C_s^* (1-k_0)}{k_0 D_L} \tag{8.12}$$

where m_L, C_s^*, k_0 and D_L are the slope of the liquidus line, the solid composition at the interface, the distribution coefficient and the diffusion coefficient in the melt, respectively. A planar front is stable only when G/R exceeds the right-hand side; as G/R falls below it the constitutional undercooling grows and the front becomes increasingly unstable, so the morphology changes in the sequence planar → cellular → dendritic → equiaxed, the G/R in additive manufacturing always being far below the value required for a planar front. Evaluating the right-hand side requires the alloy solidification parameters , *, and , which are not determined in the present thermal analysis. The solidification morphology is therefore assessed not by computing the right-hand side, but by comparing the calculated G/R — the left-hand side, obtained from the model — with G/R values reported in the literature for the same alloys. In this work the temperature gradient G at the solidification front was obtained from the build-direction thermal field of the model for each layer. Knowing G and the cooling rate CR, the solidification rate was calculated from $R = CR/G$ (from Eq. 8.11). The ratio G/R was used as the indicator of the solidification morphology, and the product $G{\cdot}R$ ($= CR$) characterizes the scale of the structure consistent with Section 8.3.2. The results are listed in Table 8.11 and shown in Figure 8.8.

Table 8.11. *Temperature gradient, solidification rate and G/R ratio of each deposited layer.*

Layer	Material	*G*, °C/mm	*R*, mm/s	*G/R*, °C·s/mm²
3	H13	215	7.88	27.3
4	H13	176	7.14	24.7
5	H13	152	6.80	22.3

Layer	Material	*G*, °C/mm	*R*, mm/s	*G/R*, °C·s/mm²
6	H13	140	6.63	21.1
7	H13	134	6.58	20.4
8	IN718	91	5.42	16.9
9	IN718	43	7.81	5.5
10	IN718	33	8.66	3.8
11	IN718	28	8.89	3.2
12	IN718	26	8.96	2.8
13	IN718	24	8.98	2.7
14	IN718	14	11.27	1.2

The temperature gradient decreases steadily up the build, from about 215 °C/mm at layer 3 to about 134 °C/mm at the top of the H13 section, and from about 91 °C/mm to 14 °C/mm through the IN718 section (Figure 8.8, top panel). The solidification rate behaves in the opposite way: it remains of the order of the scan speed (about 6.6–7.9 mm/s) in the H13 layers — a useful check, since the front at the pool tail advances at roughly the beam velocity — and rises to about 11.3 mm/s at the top of the IN718 section as the gradient collapses.

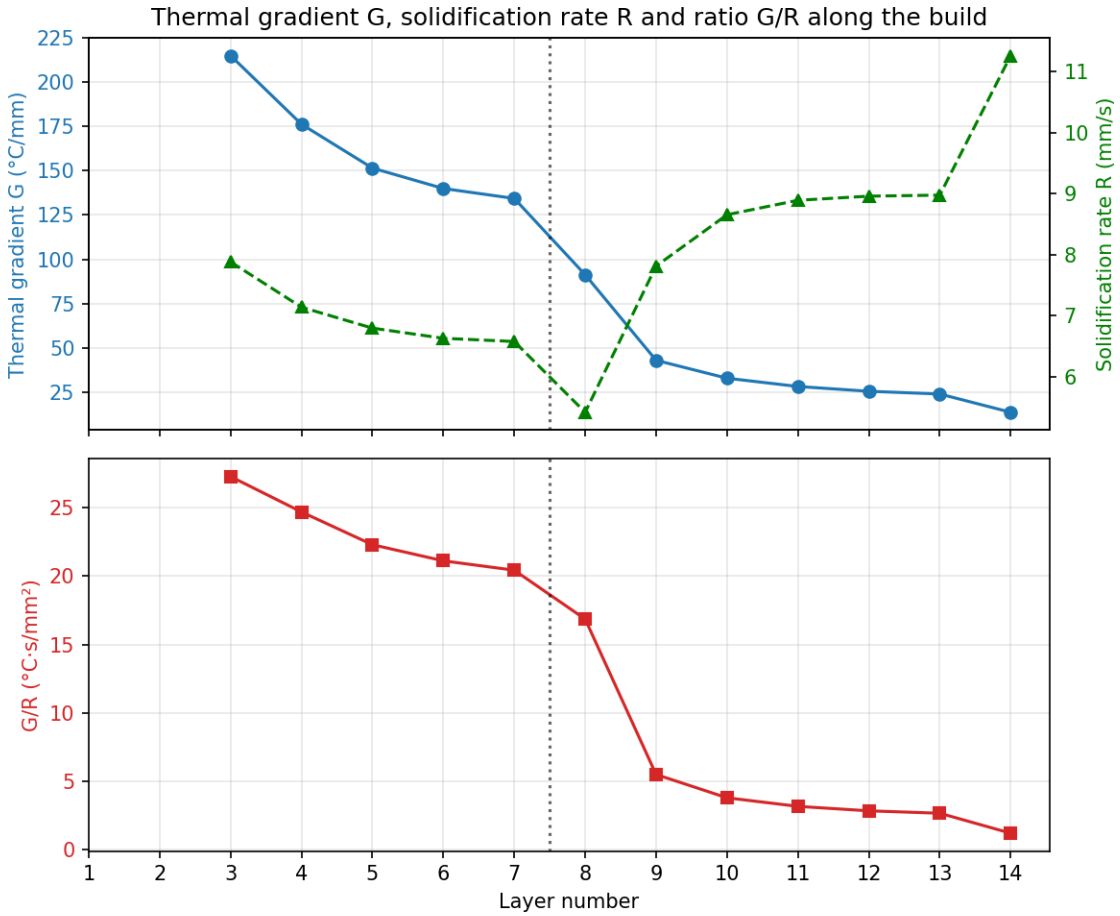

Figure 8.8. *Thermal gradient G, solidification rate R and the ratio G/R along the build.*

In the H13 section the computed *G/R* lies between about 27 and 20 °C·s/mm² (Figure 8.8, bottom panel). These values fall within the 20–140 °C·s/mm² range predicted for directed-energy-deposited H13 by Joshi et al. [23] for a comparable process, which provides an independent literature check on the present gradient extraction. In that range the as-built H13 is reported to consist of a cellular/dendritic substructure (δ-ferrite and austenite, with carbide-forming elements segregated at the cell boundaries) [25]; the H13 section here is therefore interpreted as cellular/dendritic, becoming finer and increasingly dendritic toward the top of the section as *G/R* decreases.

In the IN718 section the *G/R* values are lower, from about 17 at the first IN718 layer to about 1 °C·s/mm² at the top of the build, placing the whole section below the value of approximately 55 °C·s/mm² identified by Ghanavati et al. [14] as the transition from a cellular to a dendritic structure: the drop in *G/R* across the H13-to-IN718 boundary therefore corresponds to the change to a clearly dendritic morphology. Finally, since the product *G·R* equals the cooling rate, it decreases up the build in the same way as in Section 8.3.2, consistent with the coarsening of the dendrite arm spacing. Overall, the upper layers experience a lower gradient, a higher solidification rate and therefore a lower *G/R*, so the microstructure becomes both more dendritic and coarser toward the top of the part — a direct consequence of the heat accumulation described in Section 8.1.2.

8.4 Summary of obtainable results and scope

This chapter has presented the thermal field computed for the multi-material build and the quantities derived from it. Table 8.12 lists these quantities together with the way each was obtained. The temperature field and the geometric and rate measures taken from it — melt pool size, cooling rate, thermal gradient and solidification rate — follow directly from the simulation, whereas the microstructural indicators (solidification morphology and secondary dendrite arm spacing) and the printability assessment are obtained by post-processing the thermal results with published correlations and literature data, and should therefore be read as predictions rather than measurements. This reflects the scope of the study, which reproduced the numerical part of the reference work for an H13–IN718 combination, with H13 in place of the lower material and without an experimental programme of its own.

The principal computed values are collected in Table 8.13 as the range spanned by each material section over the build. They give a single, consistent picture of the effect of heat accumulation: as the wall grows the cooling rate and the thermal gradient fall and the solidification rate rises, so the morphology ratio *G/R* decreases and the secondary dendrite arm

spacing increases, and the structure therefore becomes coarser and more dendritic toward the top of the part. The same trend continues across the H13-to-IN718 transition. The melt-pool depth exceeds one layer thickness in every layer except the first, so sound interlayer bonding is predicted throughout the remainder of the deposit, with a possible lack-of-fusion only at the first layer.

Quantities that fall outside a thermal-only model are not addressed here and are identified as directions for future work: residual stresses and distortion, which require a coupled thermo-mechanical analysis [26]; melt-pool fluid flow, which requires a computational-fluid-dynamics model; and experimentally validated microstructure and hardness.

Table 8.12. *Quantities obtained from the present thermal model and their status.*

Quantity	How obtained	Status
Temperature field and history	Direct simulation output	Computed
Peak temperature	Per-frame field maximum	Computed
Melt-pool length / width / depth	Liquidus isotherm	Computed (measured)
Cooling rate (dT/dt)	Average slope of the T–t curve across the solidification interval	Computed (extracted)
Thermal gradient (G)	Build-direction gradient at the solidification front	Computed (extracted)
Solidification rate (R)	$R = (dT/dt) / G$	Derived
Solidification morphology	*G/R ratio compared with literature*	Predicted
Secondary dendrite arm spacing (λ)	$\lambda = b \cdot (dT/dt)^{-n}$, with literature constants	Predicted
Printability / lack-of-fusion	Melt-pool depth versus layer thickness ($d \geq h_L$)	Predicted
Thermal-strain susceptibility (ε^*)	Buckingham-π parameter from peak ΔT, melt-pool length and material data	Predicted
Composition change (vaporization)	Langmuir flux and mass balance, using peak temperature and pool area	Predicted
Residual stress / distortion	— (thermo-mechanical)	Out of scope / future
Melt-pool fluid flow	— (CFD)	Out of scope / future
Validated microstructure / hardness	— (experimental)	Out of scope / future

Table 8.13. *Principal computed quantities for each material section (ranges across the build).*

Quantity	Symbol	H13 (layers 1–7)	IN718 (layers 8–14)	Unit
Melt-pool depth	d	0.60 – 2.20	2.40 – 3.00	mm

Quantity	Symbol	H13 (layers 1–7)	IN718 (layers 8–14)	Unit
Depth-to-layer ratio	d/h_L	0.75 – 2.75	3.00 – 3.75	–
Thermal-strain parameter	ε^* ($\times 10^6$)	0.07 – 0.28	0.27 – 0.35	–
Composition change (element loss)	ΔMn / ΔCr	≤ 6.3 (Mn)	≤ 8.9 (Cr)	%
Cooling rate	dT/dt	884 – 1695	154 – 494	°C·s^{-1}
Thermal gradient	G	134 – 215	14 – 91	°C·mm^{-1}
Solidification rate	R	6.6 – 7.9	5.4 – 11.3	mm·s^{-1}
Morphology ratio	G/R	20.4 – 27.3	1.2 – 16.9	°C·s·mm^{-2}
Cooling-rate product	$G{\cdot}R$	884 – 1695	154 – 494	°C·s^{-1}
Sec. dendrite arm spacing	λ	6.9 – 8.5	6.2 – 8.8	µm

In Table 8.13 values are the range spanned by the layers of each section across the build. Layers 1 and 2 are excluded from the rate-derived quantities (cooling rate, G, R, G/R and λ), since their central nodes did not reach the liquidus; both are included in the melt-pool depth and depth-to-layer ratio (layer 1: $d = 0.60$ mm, $d/h_L = 0.75$; layer 2: $d = 1.20$ mm, $d/h_L = 1.50$). The thermal-strain and composition-change rows summarize the printability indexes of Sections 8.2.2 and 8.2.3; the manganese figure refers to the representative-temperature estimate of Table 8.7.

9 Limitations of the Model

The model reproduces the transient thermal behavior of the build well, but rests on several simplifications that define the scope of its results:

- The analysis is purely thermal, so the strain parameter ε^* of Section 8.2.2 is a relative indicator only, not the actual strain or stress. [30]
- Melt-pool fluid flow is not resolved; the Marangoni and buoyancy circulation is represented in an averaged way through the enhanced above-solidus conductivity.
- Solid-state phase transformations are not modeled — only the latent heat of fusion is included.
- The layers share nodes and are therefore treated as perfectly bonded, with no interfacial contact resistance, so lack-of-fusion is assessed only indirectly through the melt-pool depth.
- A single track per layer is modeled with one fixed set of process parameters, on an idealized thin wall.
- The highest peak temperatures contain brief, localized surface spikes from the discretized moving source; they affect ΔT and are the reason the manganese vaporization is evaluated at the representative mid-track pool temperature, with the surface-maximum value quoted only as an upper bound (Section 8.2.3).
- The vaporization results are post-processed with the Langmuir relation under an ideal-solution assumption; above the boiling point of the element the relation diverges, so the upper-bound column of Table 8.7 overestimates the manganese loss by construction.
- The microstructural indicators and the printability assessment are correlation-based predictions, not experimentally validated measurements; an experimental validation (e.g. of the secondary dendrite arm spacing) is foreseen at the publication stage.

Together, these simplifications keep the computational cost tractable while retaining the essential transient thermal physics of the process.

10 Conclusion

In the present thesis, a transient thermal numerical model for the Directed Energy Deposition of a multi-material H13–IN718 structure was developed using the finite element method (FEM). The model implemented sequential layer activation through the element birth-and-death method, a moving Goldak double-ellipsoidal heat source through a DFLUX user subroutine, an effective convection–radiation surface-film boundary condition, temperature-dependent material properties with an above-solidus conductivity enhancement to represent melt-pool convection, and multi-material assignment, all within a consistent millimeter–tonne–second unit system and realized through manual editing of the Abaqus input file.

The simulated thermal history showed a clear and progressive heat accumulation as the wall grew. The melt-pool peak temperature rose from about 1822 °C in the first layer to roughly 2472 °C at the top of the H13 section; at the transition to IN718 it decreased only slightly, to about 2397 °C — with a single material-independent heat-source efficiency, this small step is caused by the alloy properties alone, chiefly the lower liquidus of IN718 and its high effective liquid conductivity — before settling to a quasi-steady 2110–2180 °C through the IN718 layers and rising again to about 2295 °C at the final layer. The melt pool deepened steadily up the build, from 0.60 mm to 3.00 mm, so that the predicted lack-of-fusion ratio indicated sound interlayer bonding everywhere except the first layer, where the shallow pool left a thin un-melted band at the substrate interface. The thermal-strain susceptibility ε^* was largest at the final deposited layer, which combines the longest melt pool with the renewed heat build-up of the uncapped top of the wall, and its profile across the two alloys was comparatively uniform once a single efficiency was used. Selective vaporization remained limited across the build: the chromium loss in IN718 reached at most about 9 % (a change from 18.5 to about 17.1 wt%) in the hottest layers, and the manganese loss in H13, evaluated at the representative melt-pool temperature, did not exceed about 6.3 % (≈ 0.02 wt% in absolute terms), consistent with the small composition changes reported in previous studies [14], [33].

The solidification and microstructural indicators derived from this thermal field were mutually consistent and consistent with the literature. The cooling rate decreased up the build in both sections — from about 1695 °C/s to 884 °C/s in the H13 layers and from about 494 °C/s to 154 °C/s in the IN718 layers — and the secondary dendrite arm spacing accordingly coarsened from roughly 6.9 µm to 8.5 µm in H13 and from 6.2 µm to 8.8 µm in IN718. The thermal gradient fell and the solidification rate rose toward the top of the build, so that the morphology ratio G/R decreased from about 27 to about 1 °C·s·mm^{-2}, indicating a microstructure that

becomes both more dendritic and coarser toward the top of the part. The computed solidification rate remained of the order of the scan speed in the H13 section, providing an internal check on the gradient extraction, and the H13 *G/R* values fell within the 20–140 °C·s/mm² range reported for directed-energy-deposited H13 by Joshi et al. [23] and below the cellular-to-dendritic value identified by Ghanavati et al. [14] for IN718, providing independent literature validation.

Overall, the work reproduces the numerical part of the reference study for an H13–IN718 material combination, gives results that are internally consistent and in agreement with published data, and provides a validated thermal framework on which the thermo-mechanical, microstructural and experimental extensions outlined in the following chapter can be built.

11 Future Work

Several extensions could build on the present thermal model:

- A sequentially coupled thermo-mechanical analysis, using the computed temperature history, to predict residual stresses and distortion. [27]
- Phase-transformation and microstructure modeling, to obtain the phases, dendrite arm spacing and morphology directly rather than from correlations. [28]
- A melt-pool fluid-flow (CFD) model to resolve the in-pool convection now approximated by the conductivity enhancement.
- Multi-track deposition and a parametric study of laser power, scan speed and layer thickness.
- A closer study of the H13–IN718 interface, including dilution and possible intermetallic phases.
- Experimental validation through thermocouple measurements, metallography and composition mapping.

12 References

[1] DebRoy, T., et al., "Additive manufacturing of metallic components – process, structure and properties," *Progress in Materials Science*, 92 (2018) 112–224

[2] Gibson, I., Rosen, D., & Stucker, B., *Additive Manufacturing Technologies*, 2nd ed., New York, Springer, 2015

[3] Toyserkani, E., Khajepour, A., & Corbin, S., *Laser Cladding*, Boca Raton (FL), CRC Press, 2005

[4] King, W. E., et al., "Observation of keyhole-mode laser melting in laser powder-bed fusion additive manufacturing," *Journal of Materials Processing Technology*, 214 (2014) 2915–2925

[5] Tang, T., & Felicelli, S. D., "Numerical analysis of thermo-mechanical behavior of laser cladding process"

[6] Goldak, J., Chakravarti, A., & Bibby, M., "A new finite element model for welding heat sources," *Metallurgical Transactions B*, 15 (1984) 299–305

[7] Gan, Z., et al., "Experimentally validated predictions of thermal history and microhardness in laser-deposited Inconel 718 on carbon steel," *Additive Manufacturing* (2019), DOI 10.1016/j.addma.2019.03.019

[8] Dassault Systèmes, *Abaqus Documentation*

[9] Raghavan, N., et al., "Numerical modeling of heat-transfer and the influence of process parameters on tailoring the grain morphology of IN718 in electron beam additive manufacturing," *Acta Materialia* (2016)

[10] Mukherjee, T., Manvatkar, V., De, A., & DebRoy, T., "Mitigation of thermal distortion during additive manufacturing," *Scripta Materialia* (2017)

[11] Bailey, N. S., Katinas, C., & Shin, Y. C., "Laser direct deposition of AISI H13 tool steel powder with numerical modeling of solid phase transformation, hardness, and residual stresses," *Journal of Materials Processing Technology* (2017)

[12] He, X., Yu, G., & Mazumder, J., "Temperature and composition profile during double-track laser cladding of H13 tool steel," *Journal of Physics D: Applied Physics*, 43 (2010) 015502

[13] Li, L., Zhang, X., Cui, W., Liou, F., Deng, W., & Li, W., "Temperature and residual stress distribution of FGM parts by DED process: modeling and experimental validation," *International Journal of Advanced Manufacturing Technology* (2020)

[14] Ghanavati, R., Naffakh-Moosavy, H., Moradi, M., & Eshraghi, M., "Printability and microstructure of directed energy deposited SS316L-IN718 multi-material: numerical modeling and experimental analysis," *Scientific Reports* (2022)

[15] Roberts, G. A., Krauss, G., & Kennedy, R., *Tool Steels*, 5th ed., Materials Park (OH), ASM International, 1998

[16] *ASM Handbook, Volume 1: Properties and Selection: Irons, Steels, and High-Performance Alloys*, Materials Park (OH), ASM International

[17] *Superalloys (ASM Specialty Handbook)*, Materials Park (OH), ASM International (Inconel 718 nominal composition)

[18] Donachie, M. J., & Donachie, S. J., *Superalloys: A Technical Guide*, 2nd ed., Materials Park (OH), ASM International, 2002

[19] Knapp, G. L., Raghavan, N., Plotkowski, A., & DebRoy, T., "Experiments and simulations on solidification microstructure for Inconel 718 in powder bed fusion electron beam additive manufacturing," *Additive Manufacturing* (2019)

[20] Rehmer, B., Bayram, F., Ávila Calderón, L. A., Mohr, G., & Skrotzki, B., "Elastic modulus data for additively and conventionally manufactured variants of Ti-6Al-4V, IN718 and AISI 316L," *Scientific Data*, 10 (2023) 474 (dataset: BAM, Zenodo, DOI 10.5281/zenodo.7813824)

[21] Farahani, H. K., Ketabchi, M., & Zangeneh, Sh., "Determination of Johnson–Cook plasticity model parameters for Inconel 718," *Journal of Materials Engineering and Performance* (2017)

[22] *CRC Handbook of Chemistry and Physics*, Boca Raton (FL), CRC Press

[23] Joshi, S. S., Sharma, S., Mazumder, S., Pantawane, M. V., & Dahotre, N. B., "Solidification and microstructure evolution in additively manufactured H13 steel via directed energy deposition: integrated experimental and computational approach," *Journal of Manufacturing Processes*, 68 (2021) 852–866

[24] Huang, X., Kang, N., Wang, Q., El Mansori, M., & Guittonneau, F., "Wear of directed energy deposited H13 steel as a function of its graded microstructure"

[25] Lee, J., Choe, J., Park, J., Yu, J.-H., Kim, S., Jung, I. D., & Sung, H., "Microstructural effects on the tensile and fracture behavior of selective laser melted H13 tool steel under varying conditions," *Materials Characterization* (2019)

[26] Narvan, M., Ghasemi, A., Fereiduni, E., et al., "Part deflection and residual stresses in laser powder bed fusion of H13 tool steel," *Materials & Design*, 204 (2021) 109659

[27] Shatla, M., Kerk, C., & Altan, T., "Process modeling in machining. Part I: determination of flow stress data," *International Journal of Machine Tools & Manufacture*, 41 (2001) 1511–1534

[28] Schröder, J., Evans, A., Polatidis, E., Čapek, J., Mohr, G., Serrano-Munoz, I., & Bruno, G., "Understanding the impact of texture on the micromechanical anisotropy of laser powder bed fused Inconel 718," *Journal of Materials Science* (2022)

[29] Nie, L., Zhang, Y., Yuan, J., Li, Y., Gu, Y., & Zhao, L., "Parameter determination methods for Goldak heat source model in arc welding," *Research Square* (2025), preprint, DOI 10.21203/rs.3.rs-6830106/v1

[30] Mercelis, P., & Kruth, J.-P., "Residual stresses in selective laser sintering and selective laser melting," *Rapid Prototyping Journal*, 12 (2006) 254–265

[31] Roberts, I. A., et al., "A three-dimensional finite element analysis of the temperature field during laser melting of metal powders in additive layer manufacturing," *International Journal of Machine Tools & Manufacture*, 49 (2009) 916–923

[32] Michaleris, P., “Modeling metal deposition in heat transfer analyses of additive manufacturing processes,” *Finite Elements in Analysis and Design*, 86 (2014) 51–60

[33] Mukherjee, T., Zuback, J. S., De, A., & DebRoy, T., “Printability of alloys for additive manufacturing,” *Scientific Reports*, 6 (2016) 19717

[34] Zhang, G., Chen, J., Zheng, M., Yan, Z., Lu, X., Lin, X., & Huang, W., “Element vaporization of Ti-6Al-4V alloy during selective laser melting,” *Metals*, 10 (2020) 435

[35] Zheng, B., Zhou, Y., Smugeresky, J. E., Schoenung, J. M., & Lavernia, E. J., “Thermal behavior and microstructure evolution during laser deposition with laser-engineered net shaping: Part II. Experimental investigation and discussion,” *Metallurgical and Materials Transactions A*, 39 (2008) 2237–2245

[36] Flemings, M. C., “Solidification,” *Metallurgical and Materials Transactions B*, 5 (1974) 2121–2134